ENTROPY-DRIVEN PHASE TRANSITIONS IN COLLOIDS: FROM SPHERES TO ANISOTROPIC PARTICLES

MARJOLEIN DIJKSTRA

Soft Condensed Matter group, Debye Institute for Nanomaterials Science, Utrecht University, Princetonplein 5, 3584 CC Utrecht, The Netherlands

CONTENTS

I.   INTRODUCTION

Colloidal suspensions consist of solid-like particles of sizes ranging from nanometers to micrometers, which are dispersed in a fluid medium. Colloidal particles are larger than solvent molecules, but small enough to undergo Brownian motion. This highly irregular movement of the suspended particles, named after the Scottish botanist Robert Brown, is caused by the constant bombardment of the solvent molecules onto the colloidal particle surfaces. Brownian motion allows particles to explore phase space and to self-assemble into equilibrium structures, such as three-dimensional ordered crystal structures, liquid crystalline phases, and disordered fluid phases. However, they can also form non-equilibrium structures like glasses or gel-like structures. Colloidal systems behave similarly to ordinary atomic and molecular systems, and can serve as model systems for condensed matter physics. Indeed, studies on colloidal suspensions have provided us with a wealth of insight into physical phenomena such as melting, (de)mixing, freezing, nucleation, glass transitions, gelation, and structure formation, either spontaneous or externally driven by templates, gravity, or electric fields. Moreover, the much larger size of colloids compared to atoms allows for an unprecedented degree of manipulation, visualization, and control.

More importantly, recent advances in the chemical synthesis and fabrication of colloidal particles have resulted in a spectacular variety of new colloidal building blocks [1, 2] including a huge number of shape-anisotropic particles such as rods [3–5], plates [6], colloidal molecules [7, 8], bead chains [9], dumbbells [10], hollow objects, microcapsules, patchy particles [8, 11, 12], cubes [13–17], superballs [18, 19], octahedra [16, 17, 20, 21], tetrahedra [22, 23], octapods [24–26], tetrapods [27, 28], nanostars [29–31], and colloidal caps [32–34].

The main challenge is to exploit this huge variety of available colloidal building blocks and to self-assemble them into structured arrangements for advanced and functional materials and devices. The fabrication of these so-called "nanomaterials" with a well-defined structure on the scale of tens to hundreds of nanometers, makes these materials perfectly suited for the manipulation of (visible) light. Hence, colloidal crystals with lattice spacings similar to the wavelength of light are considered to be prime candidates for the fabrication of photonic bandgap materials [35–38] with potential applications in highly efficient light-emitting diodes (LEDs), solar cells, sensors, and optical computer chips. In addition, nanomaterials with the right properties are likely to be instrumental in the development of new photovoltaic cells [39, 40] and electronic displays [41, 42]. The potential use of the spontaneous self-organization of colloids as a promising and inherent cheap route for the fabrication of nanostructures requires not only the ability to tune the properties of the colloidal building blocks, but also a better understanding of the relation between the building blocks, their interactions, and the self-assembled structures.

In addition, the tunability of the effective interactions between the colloidal particles offer great opportunities. To be more specific, colloidal particles with anisotropic interactions can be synthesized by controlling the shape of the particles, or by creating "patches" on the surface of the particles. The interactions between the particles can also be altered by modifying the dispersive medium, that is, the addition of salt to the dispersion leads to screening of the electrostatic interactions, the presence of non-adsorbing polymer results in effective depletion attractions, critical Casimir forces arise due to the confinement of long-range density fluctuations when the host fluid is close to a critical point, and solvent-mediated interactions can arise when the solvent approaches a binodal. One can further modify the interaction by application of, for example, external electric and magnetic fields, templates, gravity.

Exploiting the self-assembly of these novel colloidal building blocks calls for theoretical tools to predict the structure and phase behavior of these particles. Predicting the equilibrium phase behavior of colloidal particles can be divided into three parts: (i) First, one should identify the possible "candidate" structures in which the particles with given interactions and system parameters may assemble, (ii) subsequently, the free energy of the identified candidate structures should be determined to establish the thermodynamically stable phases and to map out the full equilibrium phase diagram, and (iii) finally, one should investigate the kinetic pathways to form the thermodynamically stable phases, as the self-assembly may be suppressed by kinetic effects such as vitrification, gelation, defects, and stacking faults. In Section II and III, we describe an efficient simulation method to predict candidate structures and several techniques to calculate the free energy of the various phases. A natural starting point to study the self-assembled structures of these shape-anisotropic colloidal building blocks is to view them as hard particles [1]. Not only can these hard-particle models be used to predict properties of suitable experimental systems, but such models also provide a stepping stone toward systems where soft interactions play a role [19,43]. In addition, the analysis of hard particles is of fundamental relevance and raises problems that influence fields as diverse as (soft) condensed matter [1, 38, 44], mathematics, [45, 46] and computer science [47]. The concurrent boom in simulation studies of hard anisotropic particles is thus not surprising [44, 46, 48–58]. Finally, we present an overview and discuss phase diagrams that have been determined using free-energy calculations in Monte Carlo simulations for binary mixtures of hard spheres and hard anisotropic particles.

II.   PREDICTING CANDIDATE CRYSTAL STRUCTURES

Predicting the structures from the interactions and the shape of the colloidal building blocks alone is vital for exploiting self-assembly and a major computational challenge. In a recent review article, Woodley and Catlow [59] claimed "The
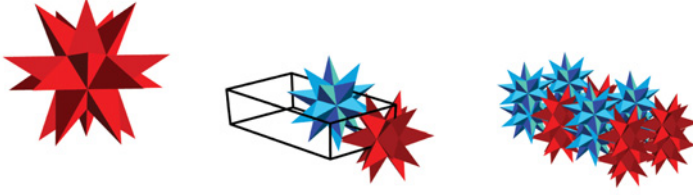
prediction of structure at the atomic level is one of the most fundamental challenges in condensed matter science," and Maddox stated in a News and Views Nature article [60] "One of the continuing scandals in the physical sciences is that it remains in general impossible to predict the structure of even the simplest crystalline solids from a knowledge of their chemical composition." Hence, it is not surprising that the subject of crystal structure prediction has received much attention from the scientific community over the last several decades. The question itself is deceivingly simple: assuming that the underlying interactions between constituent particles are known, which crystal structures are stable? Conventional methods are often based on a pre-selection of candidate structures for which the (free) energies are calculated to determine the thermodynamically most stable phase. The pre-selection of structures relies heavily on intuition, trial and error, and experience. A serious drawback of the pre-selection is that it immediately rules out all non-selected structures at the very beginning, which might include the stable equilibrium structures. Hence, it is expected that this pre-selection strategy fails dramatically for the new anisotropic colloidal building blocks for which novel and more exotic structures are envisaged.

In 1990, Pannetier et al. proposed a method based on simulated annealing techniques [61]. In their method a general crystal structure was described in terms of lattice and basis vectors, and the "cost" function for the system was minimized using simulated annealing. The method can easily be extended to any atomic system for which a suitable cost function, for example, the potential energy, can be constructed [62]. Recently, more advanced minimization techniques such as genetic algorithms [63–66] and Monte Carlo (MC) basin hopping algorithms [67] have been applied. Typically these techniques are used to locate the minimum potential energy of the system, and as such, probe the zero-temperature phase behavior. However, for systems where the entropy plays a significant role, these techniques break down. For instance, new crystal structures can appear in the phase diagram at finite temperature, which are different from the zero-temperature crystal structures, and hence predicting the zero-temperature structures will not be sufficient for making predictions at finite temperature. In addition, for hard systems the potential energy is always zero as only non-overlapping configurations contribute to the partition function, and crystal structures are thus stabilized by entropy alone. For such systems it is difficult to construct an appropriate cost function, and therefore the MC basin hopping algorithm and genetic algorithms cannot be applied to hard-core systems.

Recently, we developed a simple and efficient simulation method, which is based on a simulated annealing approach, to predict crystal structures at finite temperatures and finite pressures for a wide variety of systems, including hard-core systems whose phase behavior is purely entropy driven [49, 68, 69]. This method was applied to spheres with different types of interactions such as hard, attractive, anisotropic interactions, semi-long-range soft interactions, truly long-range interactions using Ewald sums [68], and patchy interactions [70].

In addition, the algorithm was applied to predict the best packing of a huge variety of shape-anisotropic particles [49,69]. We like to refer the interested reader to the supplementary information of Ref. [69], where we present a detailed account of the best packings of 5 Platonic solids, 13 Archimedean solids, 13 Catalan solids, 92 Johnson solids, 10 regular prisms, 10 regular antiprisms, and several nonconvex bodies. In Fig. 1, we show exemplarily these details for the best packings of hard tetrapods. This technique is similar in approach to the metadynamics method [71], but uses compression from the fluid phase and Monte Carlo (MC) sampling in

PH05: Great Stellated Dodecahedron

Model Parameters

Model file:	Great_Stellated_Dodecahedron.ply
Sphericity:	0.18759
Centrosymmetric (C/NC):	C
Upper bound to the maximum packing fraction (MPF):	1.00000
Outscribed-sphere lower bound to the MPF:	0.18806
Oriented-bounding-box lower bound to the MPF:	0.18237

Unit Cell Parameters

Number of particles:	2
Maximum packing fraction (MPF):	0.88967
Particles form a centrosymmetric compound (y/n/-):	n
Lattice Vectors:	$v1 = \{2.346500, -0.000000, -0.000000\}$
	$v2 = \{0.823346, 1.118370, -0.000000\}$
	$v3 = \{0.000551, 0.003428, 0.856627\}$

Particles in unit cell:

Index	x	y	z	Rotation Matrix		
1	1.835090	1.072080	0.479003	-0.035247	0.808356	0.587638
				-0.999343	-0.033487	-0.013877
				0.008460	-0.587741	0.809005
2	3.008070	1.070370	0.050689	-0.627904	0.621047	0.469082
				-0.472286	0.175008	-0.863897
				-0.618613	-0.763985	0.183424

Figure 1. Close-packed unit cell for the Great Stellated Dodecahedron. Adapted from the data presented in the supplementary information of Ref. [69] for the densest packings of a huge variety of anisotropic particle shapes as obtained from the "floppy-box" Monte Carlo method. For each shape we give a figure depicting the particle, the unit cell, and a small piece of the crystal, the maximum packing fraction ϕ^{UB} that we obtained, the number of particles in the unit cell, the lattice vectors, and positions and orientations of the particles in the unit cell, etc.

a variable simulation box to determine candidate structures. This technique, also referred to as the "floppy-box" Monte Carlo (FBMC) method, has proven to be remarkably efficient and robust, and has led to the discovery of an astonishing variety of new crystal structures for a wide range of systems, thereby demonstrating its effectiveness for novel colloidal building blocks that have become available experimentally [49, 68–70]. We also wish to mention other investigations of densest packings of Archimedean and Platonic solids [46, 72], hard tetrahedra [45, 73], binary hard-sphere mixtures [66, 74–77], and binary hard-disk systems [78].

The FBMC algorithm is an ordinary isothermal–isobaric (NPT) ensemble Monte Carlo (MC) simulation with three important features that makes it an efficient tool to predict candidate structures. First, the number of particles N is small, typically $1 \leq N \leq 12$. Second, the three lattice vectors $\vec{L}$ comprise the simulation box and are allowed to vary independently of each other in both their length and orientation. As in a standard NPT-MC simulation, each MC cycle consists of a trial move to displace a particle and a trial move to change the volume of the simulation box where the acceptance rules of the particle and volume moves are given by the Metropolis algorithm [79]. In order to allow for box shape fluctuations, a trial volume move involves an attempt to change the orientation and the length of a random lattice vector. This is the origin of the term "floppy box," which was adopted to emphasize that the box does not have a fixed shape. We also remark that the FBMC method is similar to other variable box shape methods [46, 71, 79], and note that an NPT variable box shape simulation is essentially an isothermal–isotension simulation with a fixed isotropic stress tensor, that is directly proportional to the pressure [79]. Third, to predict candidate structures the simulation is preceded by a compression from a disordered fluid phase. To this end, the initial pressure is chosen to be below the fluid to solid transition and the pressure is increased incrementally until the system solidifies. An essential feature of the FBMC method is that due to the small number of particles and the variable box shape, the simulation box essentially acts as a "unit cell" for the crystal structures. However, working with small simulation boxes, and allowing the shape of the simulation box to fluctuate introduce new problems. The main problem is that while the system is in the fluid phase, the shape of the box fluctuates significantly. Thus, the box can become extremely distorted, which makes the potential energy summation time consuming. To avoid this problem, one may use the lattice reduction technique as described in Ref. [65] to redraw the unit cell when it becomes too distorted. In addition, one can impose a restriction on all angles and lengths of the lattice vectors to avoid trivial unphysical crystal structures. For instance, one may exclude angles less than 30° and greater than 150°. Without these restrictions the particles tend to line up in columns, such that the particles only interact with their own periodic images in one of the lattice directions resulting in unphysical contributions to the entropy. Such a condition prevents the box (particularly while in the fluid phase) from an extreme distortion, while allowing for all possible

crystal phases to emerge in the FBMC simulations. Finally, to effectively predict candidate crystal structures it is necessary to perform FBMC simulations for the same system many times with different random seeds, starting configurations, initial conditions, compression paths, etc. This usually results in a set of candidate crystal structures for which the frequency of occurrence in the FBMC runs gives some insight into the stability of the structures [68]. In order to determine quickly whether or not a candidate structure is mechanically stable, one may perform a simulation of such a structure with a much larger system size ($\sim$1000–10,000 particles) than employed in the FBMC method. If the candidate structure deforms into another crystal structure or melts into a fluid phase, the candidate structure is thermodynamically unstable. However, we wish to remark here that only free-energy calculations can demonstrate conclusively the thermodynamic stability of candidate structures. Below, we describe in more detail how to determine the free energy for a specific structure.

III.   FREE-ENERGY CALCULATIONS

The aforementioned FBMC method and alternative algorithms can be employed to predict candidate crystal phases for a given system. Subsequently, the predicted structures can be used in free-energy calculations to determine the thermodynamically most stable phases and to map out the bulk phase diagram. Below, we describe in more detail how the free energy can be calculated in Monte Carlo simulations using the thermodynamic integration technique [79]. In this method, one constructs a reversible path that links the system of interest to a reference system for which the free energy is known. However, the free energy is known explicitly for only a few systems. To compute the Helmholtz free energy of a dense fluid, one may construct a reversible path from the system of interest to the ideal gas phase. However, for a solid, a direct path to the ideal gas without crossing a phase transition is usually not possible, and one often employs the Einstein crystal consisting of N independent harmonic oscillators as a reference state.

A.   Fluid Phase

The Helmholtz free energy for the fluid phase can be determined by integrating the equation of state (EOS), that is, the pressure as a function of density $P(\rho)$ with $\rho = N/V$ the number density, N the number of particles, and V the volume of the system. To this end, one constructs a reversible path to a dilute gas phase for which the ideal gas law $\beta P = \rho$ holds, where $\beta = 1/k_B T$, k_B equals Boltzmann's constant, T the temperature. The EOS of the fluid phase can be obtained by employing standard *NPT* Monte Carlo simulations and measuring the averaged

density ρ for a range of pressures P. The Helmholtz free energy F of the fluid phase is then determined by:

$$\frac{\beta F(\rho)}{N} = \frac{\beta F^{id}(\rho)}{N} + \int_0^\rho \left(\frac{\beta P(\rho') - \rho'}{\rho'^2} \right) d\rho', \tag{1}$$

where $\beta F^{id}(\rho)/V = \rho[\log(\rho\Lambda^3) - 1]$ is the free energy of an ideal gas at density ρ, $\Lambda = (h^2/2\pi m k_B T)^{1/2}$ denotes the de Broglie wavelength, m the mass of the particle, and h Planck's constant. Alternatively, one can also construct a reversible path to a fluid phase at density ρ_0 for which one can compute the chemical potential $\mu(\rho_0)$ using Widom's particle insertion method [79]. Using $\mu(\rho_0)$ and $P(\rho_0)$, it is straightforward to determine the Helmholtz free energy $F(\rho_0)/N = \mu(\rho_0) - P(\rho_0)/\rho_0$ at density ρ_0 [79]. The Helmholtz free energy $F(\rho)$ at density ρ can then be obtained by integrating the EOS:

$$\frac{\beta F(\rho)}{N} = \frac{\beta F(\rho_0)}{N} + \int_{\rho_0}^\rho \left(\frac{\beta P(\rho')}{\rho'^2} \right) d\rho'. \tag{2}$$

We wish to stress here that this thermodynamic integration route is not restricted to the fluid phase, but can also be employed for a solid, liquid crystalline, or any other phase, as long as we do not cross a first-order phase transition during the thermodynamic integration.

B.   Crystal Phase

The Helmholtz free energy F of a crystal phase can be calculated using the Frenkel–Ladd method [80]. Here, one constructs a reversible path from the crystal of interest to a non-interacting Einstein crystal for which one can calculate the free energy exactly. In the Einstein crystal, the centers of mass of the particles are fixed to their ideal lattice positions using harmonic springs in such a way that the particles do not interact with each other. The lattice positions of the Einstein crystal should resemble the equilibrium positions of the particles in the crystal phase of interest. The equilibrium position for each particle can be obtained by averaging the instantaneous positions of the particles in a simulation of the crystal structure. Using the Einstein crystal as a reference state, the next step is to construct a reversible path from the crystal phase to the Einstein crystal without crossing a first-order phase transition. For a system of particles that interact via hard-core potentials, one can switch on the harmonic springs, while keeping the hard-core interactions between the particles. To this end, one introduces the auxiliary Hamiltonian

$$\beta H(\mathbf{r}^N; \lambda) = \sum_{i<j}^N \beta \phi_{hc}(\mathbf{r}_i, \mathbf{r}_j) + \lambda \sum_{i=1}^N \frac{(\mathbf{r}_i - \mathbf{r}_{i,0})^2}{\sigma^2}, \tag{3}$$

where $\mathbf{r}_i$ is the center-of-mass position of particle i, $\mathbf{r}_{i,0}$ its ideal lattice position, λ is the dimensionless spring constant or coupling parameter, σ the size of the particle, which is taken to be the unit of length, and $\phi_{hc}(\mathbf{r}_i, \mathbf{r}_j)$ is the hard-core interaction between particles i and j. The usual thermodynamic integration path for hard particles consists of a gradual increase of λ from 0 (the system of interest) to λ_{max}. For sufficiently high λ_{max}, the particles are bound so strongly to their lattice sites that they do not feel each other, and the system reduces to a non-interacting Einstein crystal. Consequently, the free energy of the crystal phase $F(N, V, T)$ is then given by

$$\beta F(N, V, T) = \beta F_{\text{Einst}}(N, V, T) - \int_0^{\lambda_{max}} d\lambda \left\langle \frac{\partial \beta F}{\partial \lambda} \right\rangle, \qquad (4)$$

where the free energy of the ideal Einstein crystal $F_{\text{Einst}}(N, V, T)$ with the center-of-mass correction terms reads [79]:

$$\beta F_{\text{Einst}}(N, V, T) = -\frac{3(N-1)}{2} \ln\left(\frac{\pi}{\beta \lambda_{max}}\right) + \ln\left(\frac{\Lambda^{3N}}{\sigma^{3(N-1)} V N^{1/2}}\right). \qquad (5)$$

The integrand $\langle \partial \beta F / \partial \lambda \rangle = \left\langle \sum_{i=1}^{N} (\mathbf{r}_i - \mathbf{r}_{0,i})^2 / \sigma^2 \right\rangle$ in Eq. (4) can be calculated in an MC simulation of a system that is described by the Hamiltonian (3) for fixed values of λ in the range $\lambda \in [0, \lambda_{max}]$ with the constraint that the center of mass of the solid is fixed in order to avoid an unwanted drift of the solid in the limit $\lambda \to 0$.

If we consider anisotropic particles rather than spherical particles, the crystal phase possesses internal degrees of freedom in addition to translational degrees of freedom. In this case, each particle i possesses d configurational degrees of freedom, which we denote by a d-dimensional vector $\mathbf{q}_i$. For spherical particles in three spatial dimensions, each particle i is described by the center-of-mass position, yielding $\mathbf{q}_i \equiv \mathbf{r}_i$, and the number of degrees of freedom equals $d = 3$. Uniaxial anisotropic particles can be characterized by a unit vector $\hat{u}$ to denote the orientation of the symmetry axis, and possess two orientational degrees of freedom in addition to the translational degrees of freedom, which yield $d = 5$. Anisotropic particles without any axes of symmetry have three rotational degrees of freedom and should be described by two perpendicular unit vectors or in terms of the three Eulerian angles (θ, ϕ, χ), resulting in $d = 6$. As a consequence, the crystal phase of anisotropic particles exhibits internal degrees of freedom in addition to the translational degrees of freedom, which may give rise to a wide variety of new crystal phases. For crystal structures consisting of anisotropic particles, the thermodynamic integration route as discussed above may fail as the system will never reach the limit of a non-interacting Einstein crystal due to the orientational degrees of freedoms of the hard-core particles. In Sections III.C and III.D we

describe two methods to construct a reversible path from a crystal phase consisting of *anisotropic* particles to a non-interacting Einstein crystal.

C.   Plastic Crystal Phases

For crystal structures consisting of freely rotating anisotropic particles, the so-called plastic crystal or rotator phases, the thermodynamic integration method (4) fails if the system remains interacting even for infinite values of the spring constant λ due to the rotations of the hard-core particles. The Einstein integration method can then be combined with an additional thermodynamic integration path, which changes gradually the hard-core system into a non-interacting system. To this end, one approximates the hard-particle potential $\phi_{hc}(\mathbf{q}_i, \mathbf{q}_j)$ by an penetrable interaction potential $\varphi(i, j)$, where we use the shorthand notation $\varphi(i, j) = \varphi(\mathbf{q}_i, \mathbf{q}_j)$, where $\mathbf{q}_i$ denotes the translational and orientational degrees of freedom of particle i. The Hamiltonian is now given by:

$$\beta H(\mathbf{q}^N; \lambda, \gamma) = \gamma \sum_{i<j}^{N} \beta\varphi(i, j) + \lambda \sum_{i=1}^{N} \frac{(\mathbf{r}_i - \mathbf{r}_{i,0})^2}{\sigma^2}, \tag{6}$$

where

$$\beta\varphi(i, j) = \begin{cases} 1 - A\zeta(i, j) & 0 \le \zeta(i, j) < 1 \\ 0 & \text{otherwise} \end{cases}, \tag{7}$$

with γ the integration parameter and A an adjustable parameter, which is kept fixed during the simulation at a value of, say $A = 0.9$ [81]. In the limit $\gamma \to \infty$ the pair potential reduces to the hard-core interaction, but convergence of the thermodynamic integration is often already obtained for lower values of γ_{max}. This method allows us thus to change gradually from a non-interacting system, $\gamma = 0$, to a crystal phase of (freely rotating) hard particles when γ_{max} is sufficiently high. In order to minimize the error and maximize the efficiency of the free-energy calculations, the penetrable potential $\varphi(i, j)$ must decrease if the volume with which the particles overlap decreases and the potential must exhibit a discontinuity when the particles are just at contact [81]. In this case, the amount of overlap and the number of overlaps decrease smoothly upon increasing γ. To achieve this, one defines $\zeta(i, j)$ in such a way that it is 0, when particles i and j are fully overlapping, and 1 when particles i and j are just in contact. This thermodynamic integration path was introduced in Ref. [81] for hard spheres, and subsequently extended to hard dumbbells, hard superballs, and hard truncated cubes in Refs. [57,82,83]. For hard spheres with diameter σ, one may use $\zeta(i, j) = (r_{ij}/\sigma)^2$, which is zero when the two spheres are at center-of-mass distance $r_{ij} = |\mathbf{r}_i - \mathbf{r}_j| = 0$ and thus right on top of each other, and 1 when the particles are just in contact, that is, $r_{ij} = \sigma$ [81]. A similar approach was employed for hard dumbbells, where the individual spheres of each dumbbell interact with this penetrable pair potential [57]. In the

case of superballs, one may take $\zeta(i,j)$ to be equal to the scaling factor with which the size of particles i and j should be scaled uniformly to bring the particles just in contact provided the original positions and orientations are kept fixed [82]. With this choice, one finds again that for fully overlapping particles, $\zeta(i,j) = 0$ as the particles sizes should be scaled by 0 to remove the overlap, and $\zeta(i,j) = 1$ when the particles are just in contact.

In order to obtain the Helmholtz free energy of the crystal phase, one has to integrate over both paths to determine the free-energy difference between the system of interest and the non-interacting Einstein crystal. Starting at a very high value of $\gamma_{\max}$ where the particles behave as hard particles, one can turn on the springs that couple the particles to their respective lattice positions by increasing λ from 0 to $\lambda_{\max}$. Subsequently, one can then decrease γ from $\gamma_{\max}$ to 0 such that the system reduces to an ideal Einstein crystal. The Helmholtz free energy F of the crystal is then obtained by integrating over both paths

$$
\beta F(N, V, T) = \beta F_{\text{Einst}}(N, V, T) - \int_0^{\lambda_{\max}} d\lambda \left\langle \frac{\partial \beta F}{\partial \lambda} \right\rangle_{\gamma_{\max}}
$$
$$
+ \int_0^{\gamma_{\max}} d\gamma \left\langle \frac{\partial \beta F}{\partial \gamma} \right\rangle_{\lambda_{\max}}, \tag{8}
$$

where

$$
\langle \partial \beta F / \partial \lambda \rangle = \left\langle \sum_{i=1}^N (\mathbf{r}_i - \mathbf{r}_{0,i})^2 / \sigma^2 \right\rangle \tag{9}
$$

and

$$
\langle \partial \beta F / \partial \gamma \rangle = \left\langle \sum_{i<j}^N \beta \varphi(i,j) \right\rangle. \tag{10}
$$

We note that for particles with d_r rotational degrees of freedom, the Helmholtz free energy of a non-interacting Einstein crystal (5) includes an additional term $\sum_{k=1}^{d_r} N \ln \mathcal{V}_k$ due to the integration over the angular momenta [84]. Here, we define $\mathcal{V}_k = (h^2/2\pi I_k k_B T)^{1/2}$ with I_k the corresponding moment of inertia.

D. Orientationally Ordered Crystal Phases

For crystal structures consisting of anisotropic particles that display orientational order, one may add an aligning potential that fixes the orientations of the particles to the orientations of the ideal crystal lattice in order to reach the non-interacting

Einstein crystal [85]. Using the same coupling constant λ that attaches the particles to their lattice sites, the Hamiltonian is now given by

$$\beta H(\mathbf{q}^N; \lambda) = \lambda \sum_{i=1}^{N} \left[\frac{(\mathbf{r}_i - \mathbf{r}_{i,0})^2}{\sigma^2} + \sin^2 \psi_{i,a} + \sin^2 \psi_{i,b} \right], \qquad (11)$$

where the angles $\psi_{i,a}$ and $\psi_{i,b}$ are the minimum angles between the orientation of particle i and the respective orientations, say $\mathbf{a}$ and $\mathbf{b}$, of particle i in the ideal crystal lattice. The coupling parameter λ controls the strength of both external potentials; hence for $\lambda = 0$ the system reduces to the crystal structure of interest, and for $\lambda = \lambda_{\max}$ with $\lambda_{\max}$ sufficiently large, the system reduces to a non-interacting Einstein crystal. The Helmholtz free energy of the crystal phase can then be obtained using Eq. (4) with $\langle \partial \beta F / \partial \lambda \rangle = \langle \sum_{i=1}^{N} (\mathbf{r}_i - \mathbf{r}_{0,i})^2 / \sigma^2 + \sin^2 \psi_{i,a} + \sin^2 \psi_{i,b} \rangle$. The Helmholtz free energy of the non-interacting Einstein crystal F_{Einst} reads

$$\beta F_{\text{Einst}}(N, V, T) = -\frac{3(N-1)}{2} \ln \left(\frac{\pi}{\beta \lambda_{\max}} \right) + N \ln \left(\frac{\Lambda^3}{\sigma^3} \right)$$

$$+ \sum_{k=1}^{d_r} N \ln \mathcal{V}_k + \ln \left(\frac{\sigma^3}{V N^{1/2}} \right)$$

$$- \sum_{i=1}^{N} \ln \left[\frac{1}{8\pi^2} \int e^{-\lambda_{\max}(\sin^2 \psi_{i,a} + \sin^2 \psi_{i,b})} \sin \theta \mathrm{d}\theta \mathrm{d}\phi \mathrm{d}\chi \right], \quad (12)$$

where the latter term is the free energy due to the aligning field, which can be estimated numerically by integrating the respective partition function over all particle orientations described by the Eulerian angles θ, ϕ, and χ.

IV. BULK PHASE DIAGRAM AND KINETIC PATHWAYS

A. Mapping Out Phase Diagrams

In order to establish the thermodynamic stable phases and to determine the equilibrium phase diagram, one should first determine the Helmholtz free energy $F(N, V, T)$ of the identified candidate phases using the thermodynamic integration techniques as discussed in Section III. Since F is an extensive quantity for macroscopically large N and V, it is convenient to define a free-energy density $f(\rho, T) = F/V$. Both the pressure and the chemical potential are important quantities in the determination of phase boundaries at first-order transitions. The pressure P is given by $P(\rho, T) = -(\partial F / \partial V)_{N,T} = -f + \rho (\partial f / \partial \rho)_T$ and the chemical potential μ reads $\mu(\rho, T) = (\partial F / \partial N)_{V,T} = (\partial f / \partial \rho)_T$. The conditions for coexistence of phase I and phase II with densities ρ_I and ρ_{II} are $T^I = T^{II}$, $P^I(\rho_I) = P^{II}(\rho_{II})$, and

$\mu^I(\rho_I) = \mu^{II}(\rho_{II})$, corresponding to thermal, mechanical, and chemical equilibria, respectively. Invoking the latter two conditions at fixed temperature yields

$$\left.\frac{\partial f}{\partial \rho}\right|_{\rho_I} = \left.\frac{\partial f}{\partial \rho}\right|_{\rho_{II}} = \frac{f(\rho_{II}) - f(\rho_I)}{\rho_{II} - \rho_I}. \tag{13}$$

Geometrically this representation corresponds to the so-called common tangent construction for determining ρ_I and ρ_{II}. This is illustrated in Fig. 2, where we plot schematically the common tangent construction for a simple fluid at three different temperatures as denoted by the horizontal dashed lines in the phase diagram in Fig. 2d. At high temperature, we find a symmetry-breaking liquid–solid transition, see Fig. 2a. Figure 2b shows the existence of a symmetry-conserving
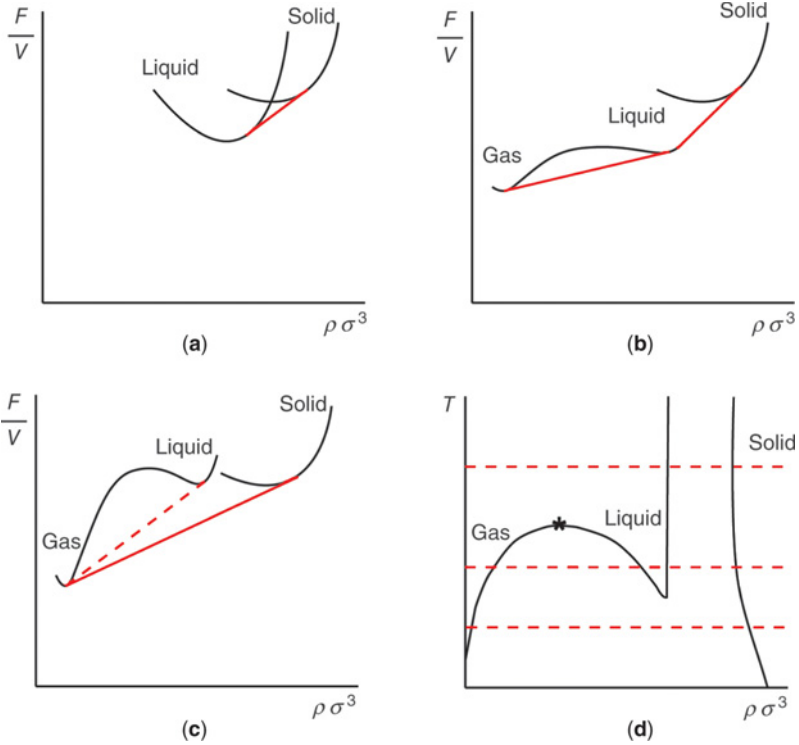

Figure 2. Schematic illustration of the common tangent construction to determine phase coexistence at varying temperatures as denoted by the horizontal dashed lines in the phase diagram in the temperature T–density $\rho\sigma^3$ representation in (**d**). The free-energy density $f = F/V$ versus the density $\rho\sigma^3$, showing (**a**) the existence of a symmetry-breaking liquid–solid transition at high temperature, (**b**) a symmetry-conserving gas–liquid transition at low densities and a symmetry-breaking liquid–solid transition at higher densities at intermediate temperature, (**c**) a metastable gas–liquid transition with respect to a stable liquid–solid transition at low temperature.

gas–liquid transition at low densities and a symmetry-breaking liquid–solid transition at higher densities at intermediate temperature. At sufficiently low temperatures, we find that the gas–liquid transition becomes metastable with respect to a broad gas–solid transition, see Fig. 2c. The physical interpretation of the common tangent construction, denoted by the linear straight solid lines in Fig. 2, shows that the system can lower its free energy by forming a linear combination of two coexisting phases. Finally it is straightforward to show that adding terms to F which are linear in ρ, does not affect the values of the bulk coexistence densities. One can make the common tangent construction with or without these terms.

B. Nucleation, Gelation, and Glass Transition

Whether or not the thermodynamically stable crystal phase will actually be formed depends also on kinetic effects. The crystallization may be suppressed by vitrification [48, 86–89] or gelation [90, 91], and may suffer from defects [92] such as stacking faults [93] and vacancies [54, 92]. It is therefore important to study also the kinetics, nucleation rates [94–96], and the various pathways for the spontaneous formation of nuclei that can grow into the thermodynamically stable phase. Such simulation studies have been carried out for binary hard-sphere mixtures [97], rod-like particles [98–104], and plate-like particles [89]. In addition, one may facilitate the formation of the ordered phases by employing external fields, like electric or magnetic fields [105–107], gravity [53, 108–112], templates [113–116], interfaces, fluid flow. This is a very active field, but outside the scope of this review.

V. PHASE DIAGRAMS OF BINARY HARD-SPHERE MIXTURES

The methods as described in Sections II, III, and IV can be employed to determine the phase behavior of colloidal systems. To illustrate this, we present an overview of the various phase diagrams that have been determined using these techniques for binary hard-sphere mixtures.

In 1957, Wood and Jacobson [117] and Alder and Wainwright [118] showed by computer simulations that a system of purely repulsive hard spheres has a well-defined melting transition. The origin of this fluid–solid transition is purely entropic and occurs because the entropy of the crystalline phase is higher than that of the fluid phase at sufficiently high densities. The location of the fluid–solid transition for hard spheres was determined using computer simulations by Hoover and Ree [119], and was revisited by Vega and Noya [120], who found that the packing fractions $\eta = N v_p / V$ of the coexisting fluid and face-centered cubic (FCC) solid phase are given by $\eta_{fluid} = 0.4915$ and $\eta_{solid} = 0.5431$, which corresponds to a pressure $\beta P \sigma^3 = 11.54$ with σ the diameter of hard spheres and $v_p = \pi \sigma^3 / 6$ the

volume of a sphere. Although the FCC phase is the most stable phase, the free-energy difference with respect to the metastable hexagonal-close-packed (HCP) structure is only very small, of the order of $10^{-3} k_B T$ per particle at the melting transition [93, 121, 122].

In addition, it was found by theory, experiments, and simulations that binary hard-sphere mixtures show extremely rich phase behavior. Phase diagrams as determined from computer simulations by Kranendonk and Frenkel revealed that starting from the pure limit, the freezing transition of a binary mixture of large and small hard spheres changes from a spindle-like transition via an azeotropic to an eutectic-like one when the diameters of the large and small spheres, σ_l and σ_s, respectively, become more dissimilar in size [123]. Phase diagrams for a size ratio $q = \sigma_s / \sigma_l = 0.95$ and 0.9425, display a spindle-like transition with a narrow coexistence between a fluid and a substitutionally disordered FCC crystal, also called a solid solution. Here "narrow" refers to the width of this coexistence region expressed in terms of the composition difference between the two coexisting phases. When the spheres become more dissimilar in size, the fluid–solid region broadens and an azeotropic point appears at a size ratio $q = 0.92$ [123]. At higher packing fractions a coexistence region between two substitutionally disordered FCC solids appears in the phase diagram for $q = 0.90$. When this miscibility gap in the solid phase intervenes with the fluid–solid coexistence the phase diagram becomes eutectic at $q \simeq 0.875$ and 0.85 [123].

Interestingly, phase diagrams of binary hard-sphere mixtures with a size ratio $q = 0.76, 0.8, 0.82$, and 0.84 as obtained from free-energy calculations in MC simulations show a stable fluid phase, a pure FCC phase of large spheres, a pure FCC of small spheres, and binary crystals with the large (L) and small (S) spheres arranged in the so-called LS_2 Laves crystal structures with atomic analogs $MgCu_2$, $MgNi_2$, and $MgZn_2$ [38, 124]. Figure 3 shows exemplarily the phase diagram of a binary hard-sphere mixture with a size ratio $q = 0.84$, displaying that the Laves phase can coexist either with a disordered fluid phase, an FCC of large spheres, or an FCC of small spheres. Although the three Laves structures have the same maximum packing fraction, the free energies of the three Laves phases are slightly different, of the order of 10^{-3} $k_B T$ per particle, with $MgZn_2$ the lowest free energy followed by $MgNi_2$ and $MgCu_2$. In the $MgCu_2$ structure, the large spheres form a diamond lattice, whereas the small spheres sit on a pyrochlore lattice. Both the diamond and pyrochlore structures possess large photonic bandgaps for moderate dielectric contrasts [38]. The self-assembly of the $MgCu_2$ structure using a binary mixture of colloidal hard spheres is a promising route to fabricate photonic crystals with a bandgap in the visible region [38]. In addition, the phase diagram for $q = 0.74$ displays only pure FCC phases.

In experiments on sterically stabilized polymethylmethacrylate (PMMA) spheres, LS_2 (atomic analog AlB_2) and LS_{13} (atomic analog $NaZn_{13}$) superlattice structures were found for $q = 0.58$ and 0.62 [125, 126]. The presence of these superlattice structures as stable phases was subsequently confirmed by
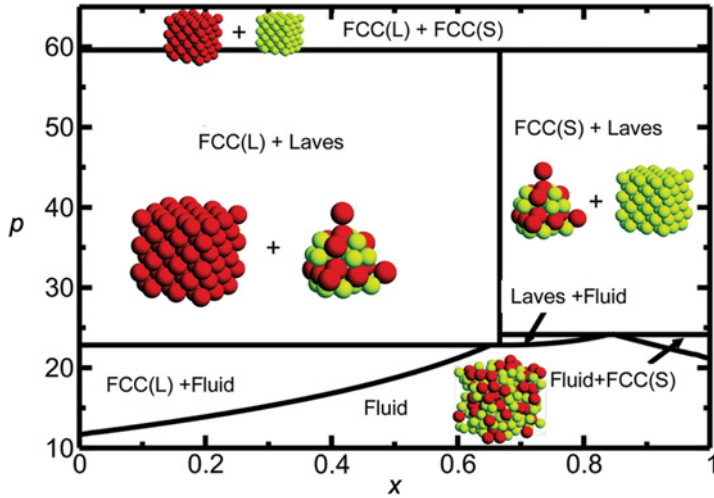
Figure 3. Phase diagram for a binary hard-sphere mixture with size ratio $q = 0.82$ in the reduced pressure p–composition x representation with $p = \beta P \sigma_L^3$, $x = N_S/(N_S + N_L)$, $N_{(S)L}$ the number of (small) large spheres, and $\sigma_{(S)L}$ the diameter of (small) large spheres. Adapted from Ref. [38]. "FCC(S)" denotes a face-centered cubic crystal of small spheres, "FCC(L)" denotes a face-centered cubic crystal of large spheres. The phase coexistence regions are labeled "FCC(L) + Laves," "FCC(S) + Laves," "Laves + Fluid," etc.

computer simulations [127, 128]. Phase diagrams of binary hard-sphere mixtures for $0.50 \leq q \leq 0.625$ display a stable fluid, a pure large-sphere FCC phase, and a small-sphere FCC phase. In addition, stable AlB_2 and $NaZn_{13}$ superlattice structures were found for $q = 0.54, 0.58$ [127], $0.59, 0.60$, and 0.61, while AlB_2 was the only stable superlattice structure for $q = 0.50$, and $NaZn_{13}$ the only one for $q = 0.625$ [128].

Furthermore, phase diagram calculations for $q = 0.414$ and 0.45 showed evidence for the thermodynamic stability of the LS (atomic analog of the NaCl rocksalt) structure, in addition to a stable fluid phase and pure FCC phases of large and small spheres [129]. An NaCl lattice is constructed by filling all octahedral holes in an FCC lattice of large particles with small particles, and hence the small spheres are also positioned on an FCC lattice. However, more recent free-energy calculations demonstrated that the coexistence region of NaCl and the pure FCC phase of big spheres is largely replaced by a so-called interstitial solid solution (ISS) for $q = 0.42$ [130]. The stoichiometry of the ISS phase is defined as LS_n where n is a fractional number in the range $[0, 1]$. Hence, $n = 0$ corresponds to a pure FCC phase and $n = 1$ to a perfect NaCl structure. A stable ISS was also found in the phase diagram for $q = 0.4$ [130] and for $q = 0.3$, which in addition displays an LS_6 structure at sufficiently high pressures [131]. We present the phase diagram for $q = 0.3$ in Fig. 4, which indeed shows that the fraction of octahedral
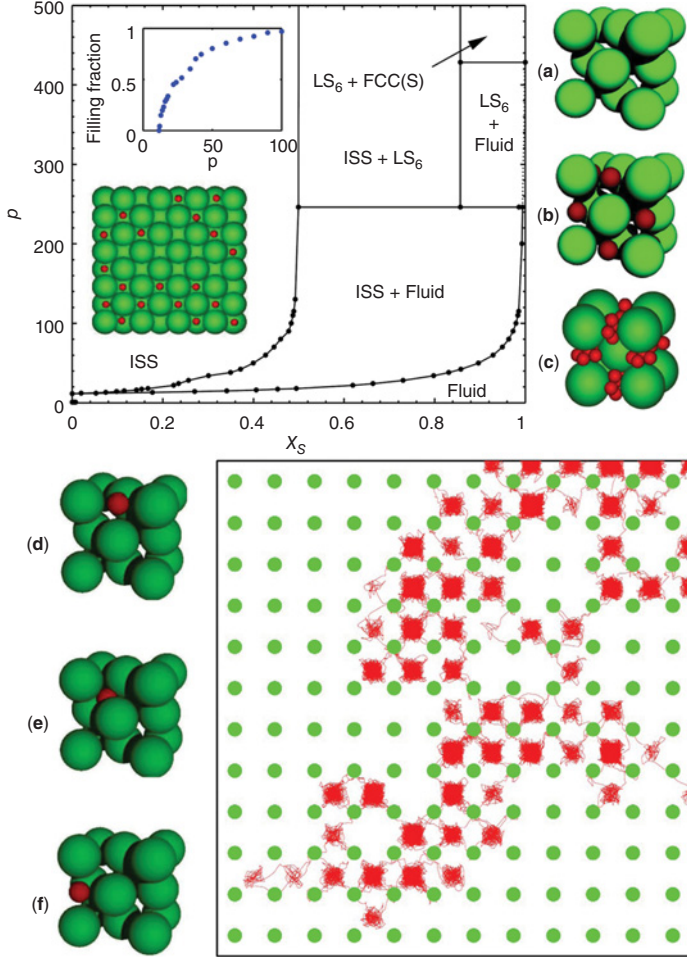
Figure 4. Phase diagram for a binary hard-sphere mixture with size ratio $q = 0.3$ in the reduced pressure p–composition x_s representation with $p = \beta P \sigma_L^3$, $x_S = N_S/(N_S + N_L)$, $N_{(S)L}$ the number of (small) large spheres, and $\sigma_{(S)L}$ the diameter of (small) large spheres [131]. The interstitial solid solution is denoted by "ISS," "FCC(S)" denotes a face-centered cubic crystal of small spheres, "FCC(L)" denotes a face-centered cubic crystal of large spheres, and "LS$_6$" denotes a binary superlattice structure. A typical configuration of the ISS phase is shown in the inset of the phase diagram. (**a**) shows a configuration of the pure FCC of large spheres, (**b**) of the NaCl phase, and (**c**) the LS$_6$ phase. The top inset in the phase diagram shows that the filling fraction of the octahedral holes in the coexisting ISS phase increases with pressure from 0 (pure FCC of large spheres) to 1 (NaCl phase). The trajectory of a single small sphere in the FCC lattice of big spheres at a volume fraction $\eta_L = 0.6$. Note that the small particle in an octahedral hole (**d**) hops first to a tetrahedral hole (**e**), and then to the next octahedral hole (**f**). Adapted from Ref. [131].

holes filled with a small sphere can be completely tuned from 0 to 1. In addition, it was observed that the small spheres diffuse throughout the lattice of the big spheres via a hopping mechanism, where the small spheres move from one octahedral hole to another via a tetrahedral hole as illustrated by the trajectory shown exemplarily in Fig. 4. Interestingly, it was also found that the diffusion increases upon increasing the density of small spheres, which is highly unexpected as in most systems the diffusion decreases with density. However, in this case, the small particles also induce an effective depletion interaction between the large spheres. Consequently, the deviations of the large particles from their ideal lattice positions increases with increasing density of the small particles due to a stronger depletion attraction between the large spheres. This in turn facilitates the hopping of small spheres in the FCC lattice of large spheres, yielding an enhanced diffusion of the small spheres [131].

Finally, the phase behavior of highly asymmetric binary hard-sphere mixtures was under debate for a long period [132]. For instance, it was unclear whether a binary fluid mixture of large and small hard spheres is miscible for all size ratios and compositions or whether a fluid–fluid demixing transition takes place. However, by integrating out the degrees of freedom of the small spheres in the partition function and using an effective Hamiltonian for the large spheres, phase diagrams of binary hard-sphere mixtures as obtained from computer simulations show a fluid–fluid transition for size ratios $q = 0.03333, 0.05$, and 0.1, but this transition is metastable with respect to a broad fluid–solid transition [132–134]. Furthermore, the stable solid phase consists of an FCC crystal of large spheres with a dispersed fluid of small spheres [132–134].

The phase behavior of binary mixtures of large and small hard spheres has been well-studied over the last decades. To summarize, we list all solid phases which are predicted to be stable in the phase diagrams of binary hard-sphere mixtures as obtained from free-energy calculations in MC simulations for various size ratios q in Table I. It is worth noting that recently the densest packing of binary hard-sphere mixtures has been investigated for a large range of stoichiometries and size ratios with up to 12 spheres in a unit cell [76,77]. A large number of crystal structures has been predicted with uncommon stoichiometries, such as LS_{11}, LS_{10}, LS_6, L_6S_6, L_3S_7, L_2S_4, which pack denser than pure FCC phases, and should be considered in free-energy calculations to determine their stability.

VI.   PHASE DIAGRAMS OF ANISOTROPIC HARD PARTICLES

We now turn our attention to phase diagrams of shape-anisotropic hard particles. An enormous amount of work has been devoted over the last decades on phase diagram calculations of anisotropic hard particles, such as spherocylinders, ellipsoids, cubes, cut spheres, oblate hard spherocylinders, dumbbells, polyhedral-shaped particles. Here we focus on phase diagrams that have been determined using

TABLE I

This Table Lists all Solid Phases Which have Been Shown to be Stable in Binary
Hard-sphere Systems as a Function of the Size Ratio $q = \sigma_s/\sigma_l$

Size Ratio (q)	Stable Phases	Reference
0.0333	FCC_L with disordered small	[132]
0.05	FCC_L with disordered small	[132]
0.1	FCC_L with disordered small	[132]
0.2	FCC_L with disordered small	[132]
0.3	FCC_L, FCC_S, ISS, NaCl, LS_6	[131]
0.4	FCC_L, FCC_S, ISS, NaCl	[130]
0.414	FCC_L, FCC_S, NaCl	[129]
0.42	FCC_L, FCC_S, ISS, NaCl	[130]
0.45	FCC_L, FCC_S, NaCl, AlB_2	[129]
0.50	FCC_L, FCC_S, AlB_2	[128]
0.54	FCC_L, FCC_S, AlB_2, $NaZn_{13}$	[128]
0.58	FCC_L, FCC_S, AlB_2, $NaZn_{13}$	[128]
0.59	FCC_L, FCC_S, AlB_2, $NaZn_{13}$	[128]
0.60	FCC_L, FCC_S, AlB_2, $NaZn_{13}$	[128]
0.61	FCC_L, FCC_S, AlB_2, $NaZn_{13}$	[128]
0.625	FCC_L, FCC_S, $NaZn_{13}$	[128]
0.74	FCC_L, FCC_S	[124]
0.76	FCC_L, FCC_S, Laves Phases ($MgZn_2$, $MgCu_2$, $MgNi_2$)	[124]
0.80	FCC_L, FCC_S, Laves Phases ($MgZn_2$, $MgCu_2$, $MgNi_2$)	[124]
0.82	FCC_L, FCC_S, Laves Phases ($MgZn_2$, $MgCu_2$, $MgNi_2$)	[124]
0.84	FCC_L, FCC_S, Laves Phases ($MgZn_2$, $MgCu_2$, $MgNi_2$)	[124]
0.85	FCC_L, FCC_S	[124]
0.85	FCC solid solution (eutectic)	[123]
0.875	FCC solid solution (eutectic)	[123]
0.90	FCC solid solution (eutectic)	[123]
0.92	FCC solid solution (azeotropic)	[123]
0.9425	FCC solid solution (azeotropic)	[123]
0.95	FCC solid solution (spindle)	[123]
1.00	FCC	[119]

*"FCC_L" denotes a pure FCC phase of large spheres, "FCC_S" a pure FCC phase of
small spheres, "FCC solid solution" is a crystal with large and small spheres randomly
distributed on an FCC lattice, "ISS" an interstitial solid solution, that is, an FCC phase
of large spheres with a fraction of the octahedral holes filled with small spheres. The
"Laves Phases" are the atomic analogs of "$MgZn_2$, $MgCu_2$, and $MgNi_2$", the "$NaZn_{13}$,
AlB_2, NaCl, LS_6" are superlattice structures for which we used their atomic analogs if
they are known. "FCC_L with disordered small" denotes an FCC lattice of large spheres
with a dispersed fluid of small spheres. In the last column, we provide the reference
that presents the full phase diagram. See also Ref. [135] for a comparison with binary
crystal structures observed in nanoparticle suspensions.

free-energy calculations instead of identifying the various phases that appear in
direct simulations. The danger of direct simulations is that systems can get trapped
in non-equilibrium structures, like gels and glasses, or in metastable ordered struc-
tures. The formation of glasses and gels, and metastable structures depends often

strongly on the history of the sample, such as the initial conditions, dynamics, and consequently, a direct approach may yield conflicting results. Moreover, for phase transitions that involve large density jumps between the coexisting phases, simulation results may suffer from finite size effects due to bulk and interfacial contributions to the free energy. For completeness, we summarize the various rigid (non-deformable or flexible) particle shapes for which the pure phase behavior (and thus not mixtures thereof) has been studied using direct simulations with or without an analysis of the EOS and various order parameters. We refer the reader to the corresponding references (and the references therein) for more details, and we stress here that this list is long but not exhaustive. Using computer simulations, the phase behavior was investigated of biaxial ellipsoids [136], hard boomerang-shaped particles [137], hard cylinders [138], hard cuboids and hard tetragonal parallelepipeds approximated by clusters of spheres [139,140], perfect hard tetragonal parallelepipeds [141], hard tetrahedra [45,55,73,142–144], contact lens-like particles [145], hard aspherical particles [146,147], six space-filling convex polyhedra namely, truncated octahedrons, rhombic dodecahedrons, hexagonal prisms, cubes, gyrobifastigiums, and triangular prisms [44], triangular bipyramids [148], truncated tetrahedra [149,150], a huge number of hard polyhedra [48,49,69], and parallel hard cubes [151]. Two-dimensional systems of hard particles were also studied by simulations, for example, hard disks [152–158], hard needles [159], hard ellipses [160], hard dimers [161], hard rods [162], hard pentagons [163], hard dominos [164], superdisks [165], and rounded hard squares [166]. In Section VI we describe the various phase diagrams that have been calculated on the basis of free-energy calculations using Monte Carlo simulations.

A.   Dumbbells

Fluid–solid equilibria of hard dumbbells consisting of two fused hard spheres of diameter σ and their centers separated by a distance L have been investigated by computer simulations in Refs. [56, 57, 167, 168]. It is convenient to introduce a shape parameter $L^* \equiv L/\sigma$ that defines the anisotropy of the dumbbell. Hence the model reduces to hard spheres for $L^* = 0$ and to tangent spheres for $L^* = 1$. Phase diagrams of hard dumbbells as determined from computer simulations by Vega showed a stable fluid phase at low packing fraction and an orientationally ordered crystal phase (CP1 phase) at sufficiently high densities [56,167,168]. For $L^* < 0.4$, a plastic crystal phase appears in the phase diagram at intermediate densities [56, 167, 168]. More recently, the phase diagram was revisited by Marechal et al., who showed that the plastic crystal with the HCP structure is more stable than the one with the FCC structure for a large part of the stable plastic crystal regime. In addition, the stability of an orientationally disordered aperiodic crystal structure is investigated. In this crystal structure, the individual spheres of the dumbbells are positioned on a random HCP lattice, and the dumbbells are oriented in random directions. We note that both the orientations as well as the centers of mass of the
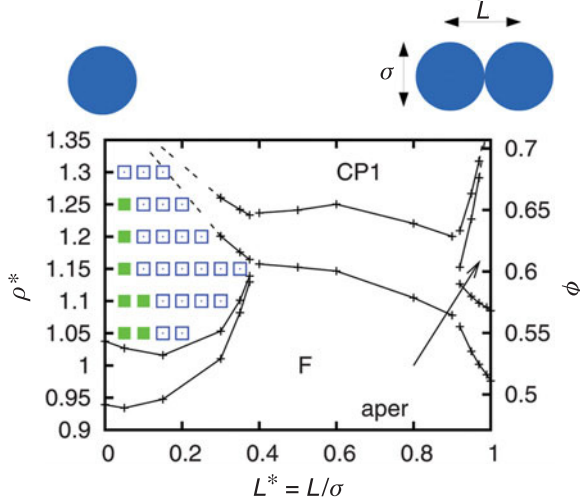
Figure 5. The phase diagram of hard dumbbells in the reduced density ρ^* (and packing fraction ϕ) versus $L^* = L/\sigma$ representation, where L is the distance between the centers of the spheres and σ is the diameter of the spheres as denoted in the schematic picture of a dumbbell [56, 57, 167, 168]. Hence the model reduces to hard spheres for $L^* = 0$ and to tangent spheres for $L^* = 1$. The dimensionless density is defined as $\rho^* = d^3 N/V$ with N the number of particles, V the volume, and $d^3/\sigma^3 = 1 + 3L^*/2 - 1/2(L^*)^3$ is the volume of a dumbbell divided by that of a sphere with diameter σ, so that d is the diameter of a sphere with the same volume as the dumbbell. "F" denotes the fluid phase and "CP1" the periodic crystal. The aperiodic phase "aper" is stable only in a narrow region of the phase diagram. The stable face-centered cubic type plastic crystal is denoted by filled squares, the hexagonal-close-packed plastic crystal phase is denoted by empty squares. Adapted from Ref. [57].

dumbbell particles are disordered in an aperiodic crystal phase. For $L^* > 0.88$, the phase diagram displays a stable aperiodic crystal phase in between the stable fluid and periodic crystal phase regimes, which is stabilized by the degeneracy or the entropy contribution due to the number of distinct bond configurations [161, 169]. Figure 5 displays the stability regimes of the plastic crystal FCC and HCP structures, and the aperiodic crystal structure.

B. Snowman-shaped Particles

The phase diagram of hard snowman-shaped particles has been calculated using Monte Carlo simulations and free-energy calculations [170]. The snowman particles consist of two hard spheres rigidly attached at their surfaces. The shape of these particles is defined by the ratio of the constituent sphere diameters $q = \sigma_s/\sigma_l$, where σ_s is the diameter of the smaller sphere and σ_l is the diameter of the larger sphere. In the limiting case of $q = 0$ the snowmen reduce to hard spheres and for $q = 1$ they reduce to hard-sphere dimers. The phase diagram presented in Fig. 6 displays rich phase behavior with isotropic, plastic crystal or rotator phase,
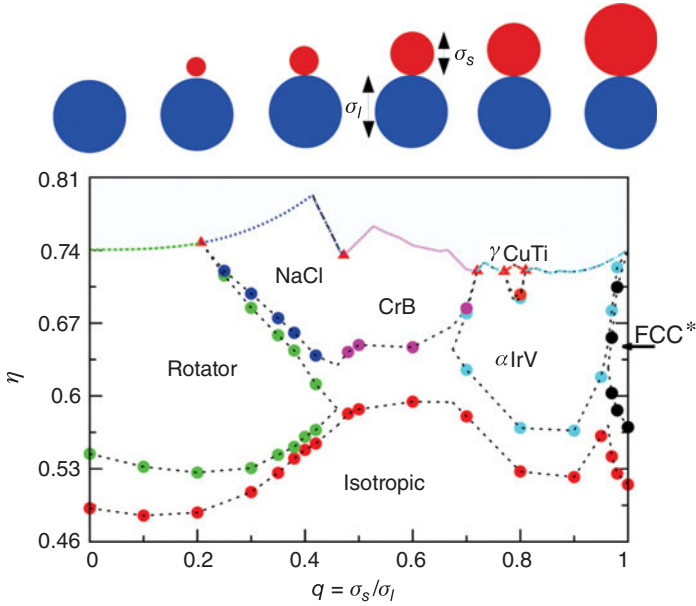
Figure 6. The phase diagram of hard snowman particles in the size ratio q–packing fraction η representation, with $q = \sigma_s/\sigma_l$ ranging from 0 (the hard sphere) to $q = 1$ (the tangential dumbbell), σ_s is the diameter of the smaller sphere and σ_l is the diameter of the larger sphere. Adapted from Ref. [170]. The packing fraction is defined as $\eta = Nv_0/V$, where v_0 is the particle volume for a given q value. Circles indicate coexisting phases, while the lines are intended to guide the eye. At the top of the plot we indicate the density of closest packing, with triangles indicating the crossover from one close-packed structure to another. "Isotropic" denotes the isotropic fluid phase, "NaCl, CrB, γCuTi, αIrV, and FCC*" denotes aperiodic crystal structures, which are stabilized by the degeneracy of the crystal structure (i.e., the number of bond configurations). "Rotator" denotes a plastic crystal phase.

and aperiodic crystal phases. In the rotator phase, the center-of-mass positions of the snowman particles are on average located on a lattice, but the particles can still rotate (although free rotation is hindered by the surrounding particles). The aperiodic crystalline phases found to be stable for a given sphere diameter ratio correspond mostly to the close-packed structures predicted for equimolar binary hard-sphere mixtures of the same diameter ratio, i.e., a structure corresponding to the atomic analog of the NaCl, CrB, γCuTi, and αIrV phases. Remarkably, these results show several crystal–crystal phase transitions, with structures with a *higher* degree of degeneracy found to be stable at lower densities, while those with the *best* packing are found to be stable at higher densities.

C. Asymmetric Dumbbell Particles

Using free-energy calculations and Monte Carlo simulations, the phase diagram of hard asymmetric dumbbell particles has been studied as a function of the distance between the centers of mass of the constituent spheres for a diameter ratio
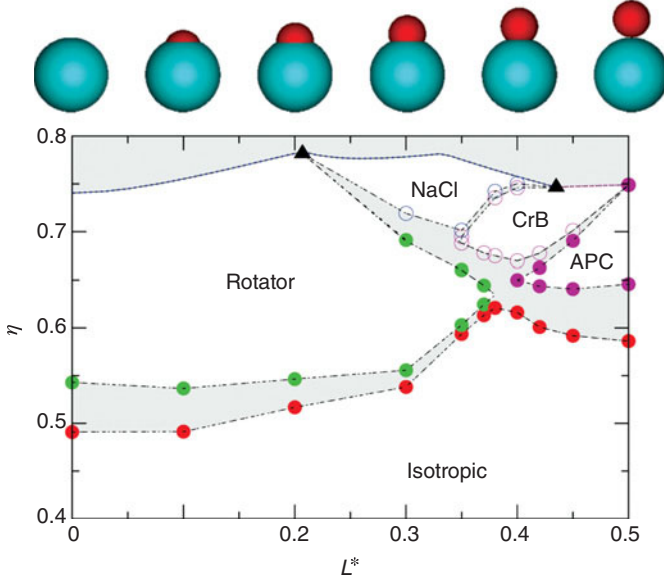
Figure 7.   The phase diagram of hard asymmetric dumbbell particles with size ratio $q = \sigma_s/\sigma_l = 0.5$ in the reduced center-of-mass distance L^*–packing fraction η representation. Adapted from Ref. [171]. The diameter of the (smaller) larger sphere is denoted by (σ_s) σ_l and the reduced center-of-mass distance is defined as $L^* = (2L + \sigma_s - \sigma_l)/2\sigma_l$ ranging from 0 (hard spheres) to 0.5 (tangential snowman-shaped particles). "APC" denotes the aperiodic CrB phase, "CrB" denotes the periodic CrB crystal, "NaCl" denotes the periodic NaCl crystal phase. Circles indicate coexisting phases, while the lines are guides to the eye. The density of the maximum packing is denoted by the line at the top of the figure, and the triangles indicate crossover points from one close-packed structure to another.

$q = \sigma_s/\sigma_l = 0.5$ with σ_s the diameter of the smaller sphere and σ_l the diameter of the larger sphere [171]. It is convenient to define the shape of the particle by the reduced sphere separation $L^* = (2L + \sigma_s - \sigma_l)/2\sigma_l$, where L is the distance between the centers of the constituent spheres and σ_l is taken to be the unit of length. L^* can be regarded as the length by which the smaller sphere protrudes from the larger one. Hence, $L^* = \sigma_s/\sigma_l$ reduces to a hard snowman-shaped particle, while for $L^* = 0$ the model reduces to a hard sphere. The phase diagram displays isotropic fluid phases, rotator or plastic crystal phases, and periodic NaCl-based and both periodic and aperiodic CrB-based crystalline phases. Aperiodic crystal phases are found to be destabilized upon reducing the sphere separation as compared to the phase diagram of snowman-shaped particles. Figure 7 shows the phase diagram for asymmetric dumbbell particles as a function of the center-of-mass distance L^* of the constituent spheres.

D.   Spherocylinders

The full phase diagram of hard spherocylinders has been mapped out by Bolhuis and Frenkel as a function of the shape anisotropy L/D [58]. A spherocylinder

consists of a cylindrical part of length L, which is capped by a hemisphere at both ends with diameter D. The phase diagram shows a stable isotropic fluid phase, liquid crystalline nematic and smectic A phases [172], orientationally ordered solid phases, which are AAA or ABC stacked, and a plastic crystal phase or rotator phase. The rotator phase is unstable for $L/D > 0.35$ and the AAA crystal phase becomes unstable for $L/D < 7$. The triple points isotropic–smectic-A–solid and isotropic–nematic–smectic-A are estimated to occur at $L/D = 3.1$ and $L/D = 3.7$, respectively. The phase diagram of the low L/D region matches remarkably well with that of hard dumbbells [56].

E.   Ellipsoids

The phase behavior of hard oblate and prolate ellipsoids of revolution was studied by Frenkel and Mulder as a function of the aspect ratio a/b [173, 174]. These authors provided evidence for a stable isotropic fluid, a nematic phase for length-to-diameter ratios $a/b \geq 2.75$ and $a/b \leq 1/2.75$, a plastic crystal for $0.8 \leq a/b \leq 1.25$, and a stretched FCC phase for sufficiently high densities. In addition, the isotropic–nematic transition has been studied using Gibbs–Duhem integration for uniaxial prolate ellipsoids [175]. More recently, a family of new structures, that is, a simple monoclinic crystal with two particles in the unit cell (SM2), has been reported [176], which yields a higher densest packing [177] and a lower free energy than the stretched FCC phases [178]. The SM2 phase is more stable than the stretched FCC structure for all densities above the solid–nematic coexistence for $a/b \geq 2.0$ [178], which was also confirmed by replica exchange Monte Carlo simulations in Ref. [179].

F.   Cut-spheres

In order to study the phase behavior of disk-shaped particles, computer simulations were carried out on systems consisting of hard cut-spheres [180]. A cut-sphere is a sphere of diameter σ with the top and bottom part of the sphere chopped off. The aspect ratio of a cut-sphere is defined by $L/\sigma > 0$, where L equals the thickness of the cut-sphere. In the case of thin hard platelets $L/\sigma = 0$, the phase diagram displays only a stable isotropic–nematic [181] and a nematic–columnar phase transition [182]. The phase diagram of hard cut-spheres displays a nematic and columnar phase for $L/\sigma = 0.1$, a columnar phase and intriguing cubatic phase for $L/\sigma = 0.2$, while a direct isotropic–solid transition was found for $L/\sigma = 0.3$ [180]. In the cubatic phase, the particles form short stacks of almost cube-like dimension, which tend to align perpendicular to each other. More recent simulations confirmed the stability of the nematic phase for $L/\sigma = 0.1$ and the stability of the cubatic phase over the nematic phase for $0.15 \leq L/D \leq 0.3$ [183]. However, the stability of the cubatic phase with respect to the columnar was inconclusive in this work [183]. In order to investigate whether or not the cubatic phase is stable with respect to the columnar phase, free-energy calculations were performed using the expanded

ensemble method [184]. Unfortunately, these calculations were also not accurate enough to provide a definitive answer. Very recently, it was shown however that the cubatic phase is metastable with respect to the isotropic–columnar phase coexistence, and can be considered as a transient glassy phase in the isotropic–columnar phase transformation [89].

G. Oblate Spherocylinders

The phase behavior of hard oblate spherocylinders as another model for plate-like particles has been investigated using free-energy calculations [53]. An oblate spherocylinder is defined by the volume within a certain distance $L/2$ to a disk of diameter D, which is analogous to the prolate spherocylinder, where the particle is defined as the volume within a certain distance from a line, see Fig. 8. The shape of oblate spherocylinders is thus more rounded due to the toroidal rim than in the case of cut-spheres, which exhibit a smooth surface with sharp edges and are thus more cylindrical in shape. The aspect ratio of an oblate spherocylinder is defined as L/σ with $\sigma = L + D$. The phase diagram of oblate hard spherocylinders as shown in Fig. 8 displays a stable isotropic phase, a nematic liquid crystal phase for $L/\sigma \leq 0.12$, a columnar phase for $L/\sigma \leq 0.3$, a tilted crystal phase for
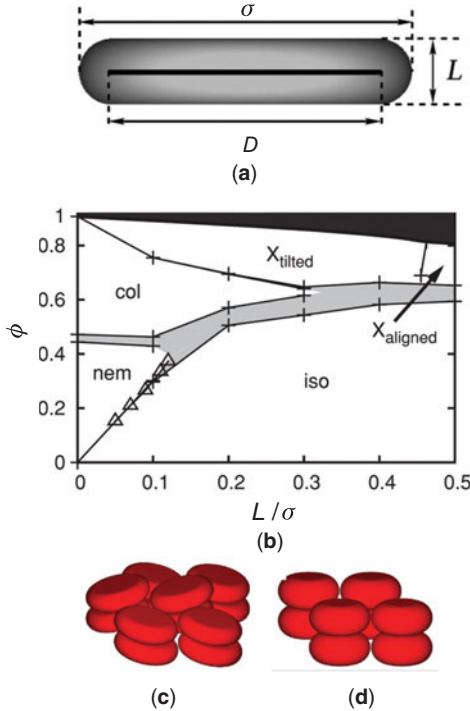

Figure 8. (**a**) Side view of an oblate spherocylinder for $L/\sigma = 0.2$, where L denotes the thickness of the plate and σ the diameter. An oblate spherocylinder is obtained by padding a disk of diameter D, as indicated by the black line, with a layer of uniform thickness $L/2$. (**b**) The phase diagram of hard oblate spherocylinders in the packing fraction ϕ–reduced thickness L/σ representation. The state points in the dark grey area are inaccessible since they lie above the maximum close packing line. "$X_{aligned}$" and "X_{tilted}" denote the aligned and tilted crystal structures as shown in (**c**) and (**d**), "iso" denotes the isotropic fluid, "nem" the nematic phase, and "col" the columnar phase. The solid lines are a guide to the eye, connecting coexistence points. The data for $L/\sigma = 0$ are taken from Ref. [182]. (**c**) The unit cell of the tilted crystal phase for $L/\sigma = 0.3$ and (**d**) the aligned crystal phase for $L/\sigma = 0.5$. Adapted from Ref. [53].

$L/\sigma \leq 0.45$, and an aligned crystal phase for $L/\sigma \geq 0.45$ [53]. The topology of the phase diagram of hard oblate spherocylinders and hard cut-spheres are quite akin. However, the tilted crystal phase for oblate hard spherocylinders, which is of a crystal type that is frequently found in experiments on disk-like molecules, has not been found for hard cut-spheres. Furthermore, the cubatic phase, which was for the first time observed in simulations on cut-spheres [180], was shown to be a transient glassy phase in the isotropic–columnar phase transformation of oblate hard spherocylinders [89]. The supersaturated isotropic phase transforms first into a cubatic phase, where the particles form short stacks that tend to orient perpendicular to each other. These locally favored structures of short particle stacks lead to geometric frustration that prevents the formation of the columnar phase and yields vitrification. In addition, it was shown that cooperative stack rotations play an important role in the devitrification process and that the lifetime of the cubatic phase can be tuned by surprisingly small differences in the particle shape [89].

H.   Cubes

Using event-driven molecular dynamics and Monte Carlo simulations, the phase behavior of hard cubes has been examined in Ref. [54]. A first-order phase transition between a fluid and a simple cubic crystal structure was found. More interestingly, it was demonstrated using free-energy calculations that the crystal phase is stabilized by a surprisingly large number of vacancies with an equilibrium vacancy concentration of approximately 6.4 % at melting, which is two orders of magnitude higher than in hard spheres. The presence of vacancies increases the positional order in the system, but also leads to appreciable diffusion in the crystal phase. Moreover, it was shown that the vacancies are delocalized over several lattice positions as illustrated in Fig. 9. Figure 9 displays the phase diagram of hard cubes and shows a stable fluid phase for $\eta < 0.45$, and a stable simple cubic crystal phase with vacancies for $\eta > 0.50$ [54]. We wish to remark here that in a previous simulation study, the ordered phase at coexistence with the liquid phase was identified to be a liquid crystalline cubatic phase, which was based on the observation of diffusion and dynamical disorder [44].

I.   Superballs

The densest packings and phase behavior of hard superballs were studied in Refs. [50–52], Recently, the full phase diagram of hard superballs was mapped out as a function of packing fraction and a shape parameter using free-energy calculations and Monte Carlo simulations [82]. A superball is defined by the inequality

$$|x|^{2q} + |y|^{2q} + |z|^{2q} \leq 1, \tag{14}$$

where x, y, and z are scaled Cartesian coordinates with q the deformation parameter. The shape of the superball interpolates smoothly between two Platonic solids,
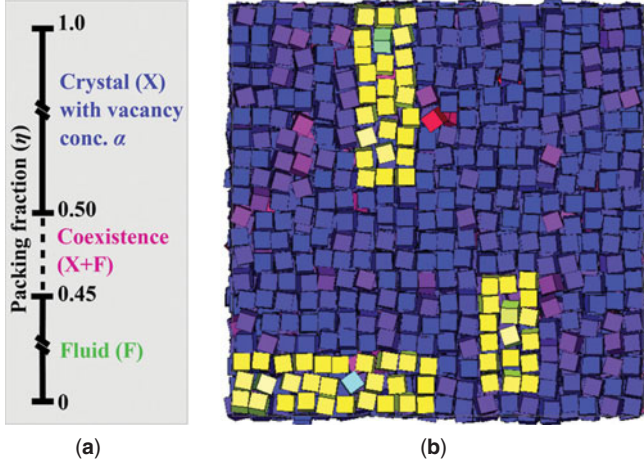
Figure 9. (a) The bulk phase diagram of hard cubes as a function of packing fraction η. A stable fluid phase is found for $\eta < 0.45$, and a stable simple cubic crystal phase with vacancies is observed for $\eta > 0.50$. Coexistence between the crystal and fluid is found for $0.45 < \eta < 0.50$. (b) A typical configuration of a simple cubic crystal phase of hard cubes at $\eta = 0.52$ and vacancy concentration of 1.6%. The particles surrounding the delocalized defects are yellow. The defect at the top has six cubes sharing seven lattice positions, the defect at the right bottom has three cubes sharing four lattice positions, and the defect at the left bottom shows seven cubes spread over eight lattice positions. Adapted from Ref. [54].

namely the octahedron ($q = 0.5$) and the cube ($q = \infty$) via the sphere ($q = 1$) as shown in Fig. 10. The phase diagram of superballs displays a stable FCC plastic crystal phase for near-spherical particles, but also a stable body-centered cubic (BCC) plastic crystal close to the octahedron shape, see Fig. 10. Moreover, phase coexistence of these two plastic crystal phases is observed with a substantial density gap. The plastic FCC and BCC crystals are, however, both unstable in the cube and octahedron limit, suggesting that the local curvature, that is, rounded corners and curved faces, of superballs plays an important role in stabilizing the rotator phases. However, the Minkowski crystal of hard octahedra always melts into a BCC plastic crystal phase before melting into the fluid phase, but free-energy calculations demonstrate that the plastic crystal phase is metastable with respect to the fluid–Minkowski crystal coexistence [82]. Furthermore, stable deformed FCC and simple cubic (SC) phases are observed in the phase diagram, which are also called C_0 and C_1 crystal phases, respectively [50, 51], as well as a body-centered tetragonal and a deformed BCC phase.

J. Bowl-shaped Particles

In addition, bowl-shaped particles have been investigated using computer simulations [90, 91]. The bowls are modeled as a solid revolution of a crescent
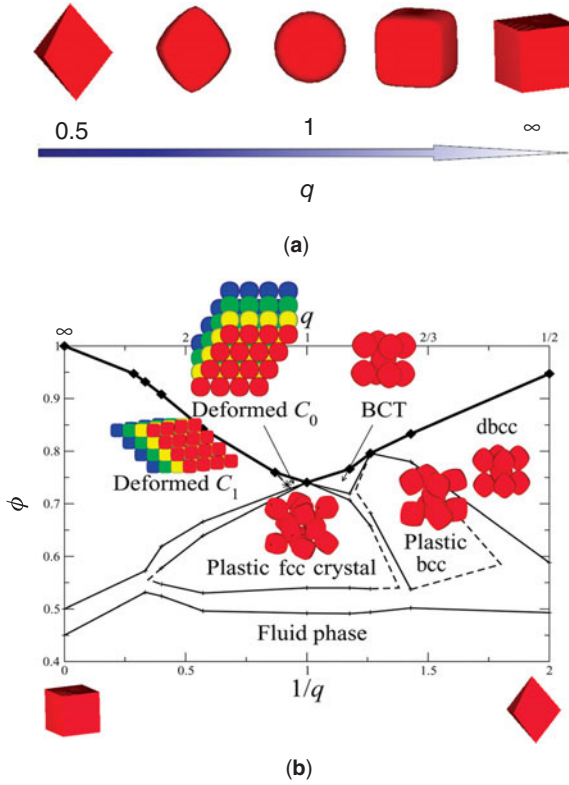
Figure 10. (a) The shape of superballs interpolates between octahedra ($q = 0.5$) and cubes ($q = \infty$) via spheres ($q = 1$). (b) The bulk phase diagram of hard superballs as a function of packing fraction ϕ versus $1/q$ (bottom axis) and q (top axis) representation where q is the shape parameter [82]. The "C_1" and "C_0" crystal phases are defined in Refs. [50, 51], where the particles of the same color are in the same layer of stacking. The solid diamonds indicate close packing, and the locations of triple points are determined by extrapolation as shown by the dashed lines. The phase boundaries for hard cubes are taken from Ref. [54]. Adapted from Ref. [82].

(see Fig. 11) with a diameter σ and a thickness D. The shape parameter of the bowl is defined as D/σ, such that the model reduces to infinitely thin hemispherical surfaces for $D/\sigma = 0$ and to solid hemispheres for $D/\sigma = 0.5$. These particles have a great tendency to form stacks due to their shape, and self-assemble spontaneously into a worm-like fluid phase. Using FBMC simulations and free-energy calculations, it was shown that the worm-like phase is a non-equilibrium phase, and that the columnar phase is more stable for sufficiently deep bowls and high densities. In addition, four exotic new crystal structures have been found. In the inverted crystal (IX), and the inverted braid-like crystal (IB), the particles are stacked in columns with half of the columns flipped upside down, such that the rims of the bowls can
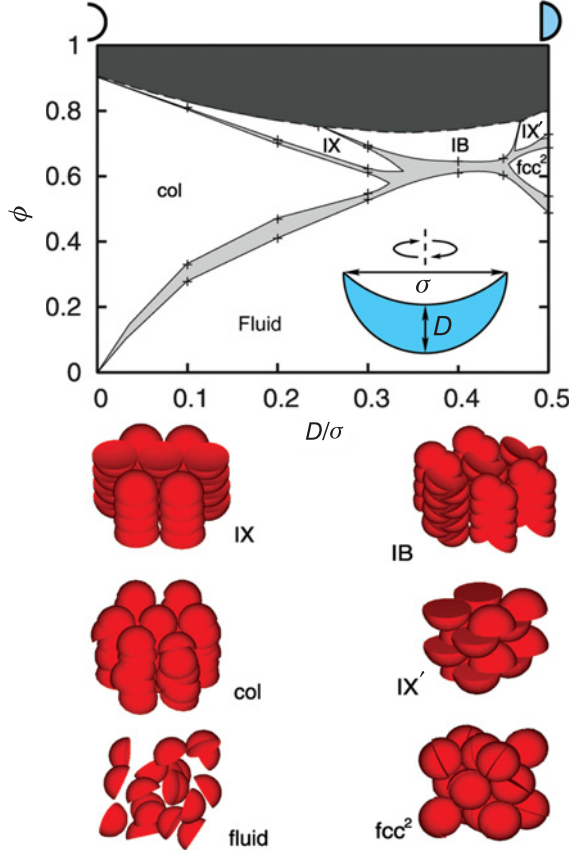
Figure 11. Phase diagram of hard bowl-shaped particles in the packing fraction (ϕ) versus thickness (D/σ) representation. Adapted from Refs. [90,91]. The light grey areas denote the coexistence regions, while the dark grey area indicates the forbidden region as it exceeds the maximum packing fraction of the bowls. The lines are a guide to the eye. The inset in the phase diagram shows the theoretical model of the bowl-shaped particle, which is the solid of revolution of a crescent around the axis as indicated by the dashed line. The thickness of the bowl is denoted by D and the diameter of the bowl by σ. The stable crystal phases, IX, IX$'$, IB, and fcc^2, the "fluid," and hexagonal columnar phase "col" are drawn schematically below the phase diagram.

interdigitate. In the IX, the columns consist of particles that are all aligned head to toe, while in the IB phase, the columns resemble braids with alternating tilt direction of the particles within each column. The solid hemispheres ($D/\sigma = 0.5$) display two stable crystal structures: the IX' phase can be regarded as a sheared version of IX with alternating orientation of the particles and where the particles are not organized in columns. In the paired face-centered cubic "fcc^2" phase, pairs of hemispheres join together to form complete spheres that can rotate freely on

the lattice positions of an fcc crystal. The phase diagram is presented in Fig. 11 as a function of shape parameter D/σ and packing fraction ϕ along with schematic pictures of the stable crystal phases [90, 91].

VII.   ENTROPY STRIKES BACK ONCE MORE

In this review article, we discussed the bulk phase behavior of a large variety of hard-particle systems. From thermodynamics we know that a bulk phase transition only occurs in a system at constant volume V and temperature T if this results in a lower Helmholtz free energy $F = U - TS$ with U the internal energy and S the entropy of the system. In most systems, a phase transition occurs because it results in a lower internal energy U and, at the same time, an increase of $-TS$. For hard-core systems, a phase transition can only occur if this results in an increase of the entropy S. At first sight, a phase transition toward a more structurally ordered phase seems at odds with our intuitive interpretation that the entropy is a measure for the disorder of a system. However, a more precise definition of the entropy, $S = k \log W$, was provided by Boltzmann, and is engraved on his grave tomb at the Zentralfriedhof in Vienna. This deceivingly simple formula that relates the entropy S to the number of accessible microstates W of a system has led to many unexpected results for the phase behavior of hard particles.

Already in the 1940s, Onsager showed that a fluid of infinitely thin hard rods exhibits an isotropic–nematic (IN) phase transition upon increasing the density [185]. In addition, computer simulations in 1957 showed a well-defined melting transition in a pure fluid of hard spheres [117, 118]. These developments showed that purely entropic (or excluded-volume) effects are sufficient to drive disorder–order transitions in the bulk, and hence one can obtain "Order through Disorder: Entropy strikes back" [186]. Many entropy-driven phase transitions have been discovered over the past few decades, like liquid crystalline phases for hard spherocylinders and ellipsoids, superlattice structures for binary hard-sphere mixtures. We presented here an overview of the various simulation studies that were focused on the determination of the phase behavior of hard-particle systems.

In addition, in order to predict the ordered structures for novel building blocks, much work has been devoted in the past years in determining the densest packings of hard-particle systems, as one might expect that the translational entropy or free volume is maximized for those structures at finite pressures. However, the packing does not solely determine which structures are more stable, and it is thus dangerous to make predictions for the phase behavior on the basis of these space filling arguments alone. For instance, the FCC and HCP phase yield the same maximum packing fraction for hard spheres, but simulations show that the FCC phase is slightly more stable than the HCP phase [93, 121, 122] due to a higher entropy associated with collective particle motions or phonon modes. In addition, we also found that not always the densest packed structures appear to be stable

in the phase diagram at finite pressures. For instance, free-energy calculations predict that the Laves phases are stable for binary hard-sphere mixtures with a size ratio $q = 0.82$ [38, 124]. However, a number of structures have been found that pack better than the more symmetric Laves phases, including αIrV, γCuTi, $AuTe_2$, and Ag_2Se. Hence, at a size ratio of 0.82 the binary hard-sphere system seems to favor the more symmetric crystal structure over the best-packed structures at finite pressures. This result should be contrasted with the AB_{13} superlattice structure for a binary hard-sphere mixture with a size ratio of $q = 0.6$. While the icosahedral AB_{13} has a lower symmetry than the cuboctahedral AB_{13}, simulations show that the better-packed icosahedral AB_{13} is more stable. In this case it appears that the system chooses the lower symmetry, but higher packed crystal structure in agreement with the space filling arguments. At finite pressures, it is thus important to examine both the close-packed structures and the related higher symmetry crystal structures, which might have a higher entropy due to lattice vibrations. This demonstrates clearly the importance of free-energy calculations in determining the phase behavior.

More surprisingly, perhaps, many examples have been found very recently that entropy can also lead to disorder in the self-assembled ordered structures. A remarkable example is that in the case of large and small hard spheres, the NaCl structure, which is the densest packed structure for an equimolar binary hard-sphere mixture with a diameter ratio of about 0.3, is replaced by a so-called ISS at finite pressures [131]. Instead of ordering both species on the corresponding sublattices, only the larger species are nicely ordered on an FCC lattice, whereas the sublattice of the smaller species exhibits a high number of vacancies leading to a highly disordered sublattice with appreciable diffusion. The system prefers thus a truly "interstitial" solution to the problem of maximizing entropy by favoring "disorder" in "order." Another intriguing example of disorder in an ordered crystal structure is a system of hard cubes [54]. In this case, the simple cubic crystal phase of hard cubes is stabilized by a surprisingly high number of vacancies, reaching a vacancy concentration of about 6.4 % at bulk coexistence. These vacancies are delocalized, result in fluid-like behavior over the delocalization length of the defect, and give rise to pronounced diffusion. Here, the system maximizes its entropy by the formation of a simple cubic crystal phase with long-range positional and orientational order, but with substantial disorder in the crystal lattice due to the presence of delocalized vacancies. Again the total entropy of the system is maximized by "disorder" in an ordered crystalline structure. As a final example, we would like to mention that in the case of hard (asymmetric) dumbbell particles and snowman-shaped particles, the system can freeze into an aperiodic crystal, in which not only the orientations but also the centers of mass of the particles are disordered. However, the constituent spheres of the particles are positioned on a periodic crystal lattice [57, 170, 171]. The aperiodic crystal is here stabilized by the degeneracy or the number of ways that the spheres can be connected to form a dimer particle. Moreover, it was also shown that even less densely packed

structures with a higher degeneracy (number of bond configurations) can be found to be stable at lower pressures, while at higher pressures the close-packed structures with a lower degree of degeneracy become stable [170].

To summarize, there are many examples where entropy alone can drive a disorder–order transition in hard-particle systems, and thus one can achieve "order through disorder" [186]. In this review article, we have summarized several of these entropy-driven phase transitions that have been investigated over the past decades. More surprisingly, it was demonstrated recently that a system can also settle for a compromise by introducing "disorder" in the ordered structures. Explicit free-energy calculations indeed prove that disorder due to vacancies or different bond orientations in the crystalline structures may increase the total entropy of the system. The subtle role that entropy plays in these entropy-driven phase transitions demonstrates clearly the importance of free-energy calculations in simulation studies on hard-particle systems. In order to conclude, one can thus obtain "Disorder in Order through Disorder," and "Entropy strikes back once more."

ACKNOWLEDGMENTS

REFERENCES

1. S.C. Glotzer and M.J. Solomon, *Nat. Mater.* **6**, 557 (2007).

2. S. Sacanna and D.J. Pine, *Curr. Opin. Colloid Interface Sci.* **16**, 96 (2011).

3. C.C. Ho, A. Keller, J.A. Odell, and R.H. Ottewill, *Colloid Polym. Sci.* **271**, 469 (1993).

4. C.M. van Kats, P.M. Johnson, J.E.A.M. van den Meerakker, and A. van Blaaderen, *Langmuir* **20**, 11201 (2004).

5. A. Kuijk, A. van Blaaderen, and A. Imhof, *J. Am. Chem. Soc.* **133**, 2346 (2011).

6. A.M. Wierenga, T.A.J. Lenstra, and A.P. Philipse, *Colloids Surfaces A.: Physicochem. Eng. Aspects* **134**, 8582 (1998).

7. A. Perro, E. Duguet, O. Lambert, J.-C. Taveau, E. Bourgeat-Lami, and S. Ravaine, *Angew. Chem.* **424**, 361 (2009).

8. D.J. Kraft, W.S. Vlug, A. van Kats, C.M. van Blaaderen, A Imhof, and W.K. Kegel, *J. Am. Chem. Soc.* **131**, 1182 (2009).

9. H.R. Vutukuri, A.F. Demirörs, B. Peng, P.D.J. van Oostrum, A. Imhof, and A. van Blaaderen, *Angew. Chem. Int. Ed.* **51**, 11249 (2012).

10. P.M. Johnson, C.M. van Kats, and A. van Blaaderen, *Langmuir* **21**, 11510 (2005).

11. D.J. Kraft, R. Ni, F. Smallenburg, M. Hermes, K. Yoon, D.A. Weitz, A. van Blaaderen, J. Groenewold, M. Dijkstra, and W.K. Kegel, *Proc. Nat. Acad. Sci.* **109**, 10787 (2012).

12. D. J. Kraft, J. Groenewold, and W. K. Kegel, *Soft Matter* **5**, 3823 (2009).

13. Y. Sun and Y. Xia, *Science* **298**, 2176 (2002).

14. X. Zhang, C. Dong, J. Zapien, S. Ismathullakhan, Z. Kang, J. Jie, X. Zhang, J. Chang, C.-S. Lee, and S.-T. Lee, *Angew. Chem. Int. Ed.* **48**, 9121 (2009).

15. H.-L. Wu, C.-H. Kuo, and M.H. Huang, *Langmuir* **26**, 12307 (2010).

16. J. Henzie, M. Grünwald, A. Widmer-Cooper, P.L. Geissler, and P. Yang, *Nat. Mater.* **11**, 131 (2011).

17. M. Eguchi, D. Mitsui, H. Wu, R. Sato, and T. Teranishi, *Langmuir* **28**, 9021 (2012).

18. L. Rossi, S. Sacanna, W.T.M. Irvine, P.M. Chaikin, D.J. Pine, and A.P. Philipse, *Soft Matter* **7**, 4139 (2011).

19. Y. Zhang, F. Lu, D. van der Lelie, and O. Gang, *Phys. Rev. Lett.* **107**, 135701 (2011).

20. A. Tao, P. Sinsermsuksakul, and P. Yang, *Angew. Chem. Int. Ed.* **45**, 4597 (2006).

21. A.R. Tao, S. Habas, and P. Yang, *Small* **4**, 310 (2008).

22. F. Kim, S. Connor, H. Song, T. Kuykendall, and P. Yang, *Angew. Chem.* **116**, 3759 (2004).

23. E.C. Greyson, J.E. Barton, and T.W. Odom, *Small* **2**, 368 (2006).

24. S. Deka, K. Miszta, D. Dorfs, A. Genovese, G. Bertoni, and L. Manna, *Nano Lett.* **10**, 3770 (2010).

25. R. Brescia, K. Miszta, D. Dorfs, L. Manna, and G. Bertoni, *J. Phys. Chem. C* **115**, 20128 (2011).

26. K. Miszta, J. de Graaf, G. Bertoni, D. Dorfs, R. Brescia, S. Marras, L. Ceseracciu, R. Cingolani, R. van Roij, M. Dijkstra, and L. Manna, *Nat. Mater.* **10**, 872 (2011).

27. L. Manna, D.J. Milliron, A. Meisel, E.C. Scher, and A.P. Alivisatos, *Nat. Mater.* **2**, 382 (2003).

28. M.C. Newton and P. A. Warburton, *Mater. Today* **10**, 1369 (2007).

29. G. Zhou, M. Lü, Z. Xiu, S. Wang, H. Zhang, Y. Zhou, and S. Wang, *J. Phys. Chem. B* **110**, 6543 (2006).

30. N. Zhao and L.M. Qi, *Adv. Mater.* **18**, 359 (2006).

31. T. Huang, Q.A. Zhao, J.Y. Xiao, and L.M. Qi, *ACS Nano* **4**, 4707 (2010).

32. C.I. Zoldesi and A. Imhof, *Adv. Mater.* **17**, 924 (2005).

33. D. Jagadeesan, U. Mansoori, P. Mandal, A. Sundaresan, and M. Eswaramoorthy, *Angew. Chem.* **47**, 7685 (2008).

34. C. Quilliet, C. Zoldesi, C. Riera, A. van Blaaderen, and A. Imhof, *Eur. Phys. J. E* **27**, 13 (2008).

35. E. Yablonovitch, *Phys. Rev. Lett.* **58**, 2059 (1987).

36. S. John, *Phys. Rev. Lett.* **58**, 2486 (1987).

37. Y.A. Vlasov, X.Z. Bo, J.C. Sturm, and D.J. Norris, *Nature* **414**, 289 (2001).

38. A.-P. Hynninen, J.H.J. Thijssen, E.C.M. Vermolen, M. Dijkstra, and A. van Blaaderen, *Nat. Mater.* **6**, 202 (2007).

39. A. Mihi, F.J. López-Alcaraz, and H. Míguez, *Appl. Phys. Lett.* **88**, 193110 (2006).

40. P. Bermel, C. Luo, L. Zeng, L.C. Kimerling, and J.D. Joannopoulos, *Opt. Express* **15**, 16986 (2007).

41. H. Qi and T. Hegmann, *J. Mater. Chem.* **18**, 3288 (2008).

42. H. Fudouzi and Y. Xia, *Langmuir* **19**, 9653 (2003).

43. A. Yethiraj and A. van Blaaderen, *Nature* **421**, 513 (2003).

44. U. Agarwal and F.A. Escobedo, *Nat. Mater.* **10**, 230 (2011).

45. E.R. Chen, M. Engel, and S.C. Glotzer, *Discrete Comput. Geom.* **44**, 253 (2010).

46. S. Torquato and Y. Jiao, *Nature* **460**, 876 (2009).

47. T.C. Hales, *Discrete Comput. Geom.* **36**, 5 (2006).

48. P.F. Damasceno, M. Engel, and S.C. Glotzer, *Science* **337**, 453 (2012).

49. J. de Graaf, R. van Roij, and M. Dijkstra, *Phys. Rev. Lett.* **107**, 155501 (2011).

50. Y. Jiao, F.H. Stillinger, and S. Torquato, *Phys. Rev. E* **79**, 041309 (2009).

51. Y. Jiao, F.H. Stillinger, and S. Torquato, *Phys. Rev. E* **84**, 069902 (2011).

52. R.D. Batten, F.H. Stillinger, and S. Torquato, *Phys. Rev. E* **81**, 061105 (2010).

53. M. Marechal, A. Cuetos, B. Martinez-Haya, and M. Dijkstra, *J. Chem. Phys.* **134**, 094501 (2011).

54. F. Smallenburg, L. Filion, M. Marechal, and M. Dijkstra, *Proc. Nat. Acad. Sci.* **109**, 17886 (2012).

55. A. Haji-Akbari, M. Engel, A.S. Keys, X. Zheng, R.G. Petschek, P. Palffy-Muhoray, and S.C. Glotzer, *Nature* **462**, 773 (2009).

56. C. Vega and P.A. Monson, *J. Chem. Phys.* **107**, 2696 (1997).

57. M. Marechal and M. Dijkstra, *Phys. Rev. E* **77**, 061405 (2008).

58. P. Bolhuis and D. Frenkel, *J. Chem. Phys* **106**, 666 (1997).

59. S.M. Woodley and R. Catlow, *Nat. Mater.* **7**, 937 (2008).

60. J. Maddox, *Nature* **335**, 201 (1988).

61. J. Pannetier, J. Bassas-Alsina, J. Rodriguez-Carvajal, and V. Caignaert, *Nature* **346**, 343 (1990).

62. H.R. Karfunkel and R.J. Gdanitz, *J. Comput. Chem.* **13**, 1171 (1992).

63. A.R. Oganov and C.W. Glass, *J. Chem. Phys.* **124**, 244704 (2006).

64. D.P. Stucke and V.H. Crespi, *Nano Lett.* **3**, 1183 (2003).

65. D. Gottwald, G. Kahl, and C.N. Likos, *J. Chem. Phys.* **122**, 204503 (2005).

66. L. Filion and M. Dijkstra, *Phys. Rev. E* **79**, 046714 (2009).

67. D.J. Wales and H.A. Scheraga, *Science* **285**, 1368 (1999).

68. L. Filion, M. Marechal, B. van Oorschot, D. Pelt, F. Smallenburg, and M. Dijkstra, *Phys. Rev. Lett.* **103**, 188302 (2009).

69. J. de Graaf, L. Filion, M. Marechal, R. van Roij, and M. Dijkstra, *J. Chem. Phys.* **137**, 214101 (2012).

70. E. Bianchi, G. Doppelbauer, L. Filion, M. Dijkstra, and G. Kahl, *J. Chem. Phys.* **136**, 214102 (2012).

71. A. Martoňák, R. Laio and M. Parrinello, *Phys. Rev. Lett.* **90**, 075503 (2003).

72. S. Torquato and Y. Jiao, *Phys. Rev. E* **80**, 041104 (2009).

73. S. Torquato and Y. Jiao, *Phys. Rev. E* **81**, 041310 (2010).

74. J.K. Kummerfeld, T.S. Hudson, and P. Harrowell, *J. Phys. Chem. B Lett.* **112**, 10773 (2008).

75. P.I. O'Toole and T.S. Hudson, *J. Phys. Chem. C* **115**, 19037 (2011).

76. A.B. Hopkins, Y. Jiao, F.H. Stillinger, and S. Torquato, *Phys. Rev. Lett.* **107**, 125501 (2011).

77. A.B. Hopkins, F.H. Stillinger, and S. Torquato, *Phys. Rev. E* **85**, 021130 (2012).

78. C.N. Likos and C.L. Henley, *Phil. Mag. B* **68**, 85 (1993).

79. D. Frenkel and B. Smit, *Understanding Molecular Simulation: From Algorithms to Applications*, 2nd edition, Academic Press (London), 2002.

80. D. Frenkel and A.J.C. Ladd, *J. Chem. Phys.* **81**, 3188 (1984).

81. A. Fortini, M. Dijkstra, M. Schmidt, and P.P.F. Wessels, *Phys. Rev. E* **71**, 051403 (2005).

82. R. Ni, A.P. Gantapara, J. de Graaf, R. van Roij, and M. Dijkstra, *Soft Matter* **8**, 8826 (2012).

83. A.P. Gantapara, J. de Graaf, R. van Roij, and M. Dijkstra, *Phys. Rev. Lett.* **111**, 015501 (2013).

84. M.P. Allen, G.T. Evans, D. Frenkel, and B.M. Mulder, *Adv. in Chem. Phys.* **86**, 1 (1993).

85. E.G. Noya, C. Vega, J.P.K. Doye, and A.A. Louis, *J. Chem. Phys.* **127**, 054501 (2007).

86. P.N. Pusey, E. Zaccarelli, C. Valeriani, E. Sanz, W.C.K. Poon, and M.E. Cates, *Phil. Trans. R. Soc. A* **367**, 4993 (2009).

87. E. Zaccarelli, C. Valeriani, E. Sanz, W.C.K. Poon, M.E. Cates, and P.N. Pusey, *Phys. Rev. Lett.* **103**, 135704 (2009).

88. E. Sanz, C. Valeriani, E. Zaccarelli, W.C.K. Poon, P.N. Pusey, and M.E. Cates, *Phys. Rev. Lett.* **106**, 215701 (2011).

89. M. Marechal, A. Patti, M. Dennison, and M. Dijkstra, *Phys. Rev. Lett.* **108**, 206101 (2012).

90. M. Marechal, R.J. Kortschot, A.F. Demirörs, A. Imhof, and M. Dijkstra, *Nano Lett.* **10**, 1907 (2010).

91. M. Marechal and M. Dijkstra, *Phys. Rev. E* **82**, 031405 (2010).

92. S. Pronk and D. Frenkel, *J. Phys. Chem. B* **105**, 6722 (2001).

93. S. Pronk and D. Frenkel. *J. Chem. Phys.* **110**, 4589 (1999).

94. L. Filion, M. Hermes, R. Ni, and M. Dijkstra, *J. Chem. Phys.* **133**, 244115 (2010).

95. S. Auer and D. Frenkel, *Nature* **409**, 1020 (2001).

96. R. Ni and M. Dijkstra, *J. Chem. Phys.* **134**, 034501 (2011).

97. R. Ni, F. Smallenburg, L. Filion, and M. Dijkstra, *Mol. Phys.* **109**, 1213 (2011).

98. A. Cuetos and M. Dijkstra, *Phys. Rev. Lett.* **98**, 095701 (2007).

99. A. Cuetos, R. van Roij, and M. Dijkstra, *Soft Matter* **4**, 757 (2008).

100. A. Cuetos, E. Sanz, and M. Dijkstra. *Faraday Discuss.* **144**, 253 (2010).

101. A. Patti and M. Dijkstra. *Phys. Rev. Lett.* **102**, 128301 (2009).

102. R. Ni, S. Belli, R. van Roij, and M. Dijkstra, *Phys. Rev. Lett.* **105**, 088302 (2010).

103. T. Schilling and D. Frenkel, *Phys. Rev. Lett.* **92**, 085505 (2004).

104. D. Frenkel and T. Schilling, *Phys. Rev. E* **66**, 041606 (2002).

105. F. Smallenburg and M. Dijkstra, *J. Chem. Phys.* **132**, 204508 (2010).

106. A.-P. Hynninen and M. Dijkstra, *Phys. Rev. Lett.* **94**, 138303 (2005).

107. A.-P. Hynninen and M. Dijkstra, *Phys. Rev. E* **72**, 051402 (2005).

108. M. Marechal and M. Dijkstra, *Soft Matter* **7**, 1397 (2011).

109. M. Marechal and M. Dijkstra, *Phys. Rev. E* **75**, 061404 (2007).

110. T. Biben, R. Ohnesorge, and H. Löwen, *Europhys. Lett.* **28**, 665 (1994).

111. T. Biben, J.-P. Hansen, and J.-L. Barrat, *J. Chem. Phys.* **98**, 7330 (1993).

112. S.V. Savenko and M. Dijkstra, *Phys. Rev. E* **70**, 051401 (2004).

113. M. Hermes, E.C.M. Vermolen, M.E. Leunissen, D.L.J. Vossen, P.D.J. van Oostrum, M. Dijkstra, and A. van Blaaderen, *Soft Matter* **7**, 4517 (2011).

114. A. Cacciuto and D. Frenkel, *Phys. Rev. E* **72**, 041604 (2005).

115. M. Heni and H. Löwen, *J. Phys.: Condens. Matt.* **13**, 4675 (2001).

116. M. Heni and H. Löwen, *Phys. Rev. Lett.* **85**, 3668 (2000).

117. W.W. Wood and J.D. Jacobson, *J. Chem. Phys.* **27**, 1207 (1957).

118. B.J. Alder and T.E. Wainwright, *J. Chem. Phys.* **27**, 1208 (1957).

119. W.G. Hoover, *J. Chem. Phys.* **49**, 3609 (1968).

120. C. Vega and E.G. Noya, *J. Chem. Phys.* **127**, 154113 (2007).

121. P.G. Bolhuis, D. Frenkel, S.C. Mau, and D.A. Huse, *Nature* **388**, 235 (1997).

122. A.D. Bruce, N.B. Wilding, and G.J. Ackland, *Phys. Rev. Lett.* **79**, 3002 (1997).

123. W.G.T. Kranendonk and D. Frenkel, *Mol. Phys.* **72**, 679 (1991).

124. A.-P. Hynninen, L. Filion, and M. Dijkstra, *J. Chem. Phys.* **131**, 064902 (2009).

125. P. Bartlett, R.H. Ottewill, and P.N. Pusey, *J. Chem. Phys.* **93**, 1299 (1990).

126. P. Bartlett, R.H. Ottewill, and P.N. Pusey, *Phys. Rev. Lett.* **68**, 3801 (1992).

127. M.D. Eldridge, P.A. Madden, and D. Frenkel, *Nature* **365**, 35 (1993).

128. M.D. Eldridge, P.A. Madden, and D. Frenkel, *Mol. Phys.* **84**, 395 (1995).

129. E. Trizac, M.D. Eldridge, and P.A. Madden, *Mol. Phys.* **90**, 675 (1997).

130. L. Filion. Self-assembly in colloidal hard-sphere systems. PhD thesis, Utrecht University, 2011.

131. L. Filion, M. Hermes, R. Ni, E.C.M. Vermolen, A. Kuijk, C.G. Christova, J.C.P. Stiefelhagen, T. Vissers, A. van Blaaderen, and M. Dijkstra, *Phys. Rev. Lett.* **107**, 168302 (2011).

132. M. Dijkstra, R. van Roij, and R. Evans, *Phys. Rev. E* **59**, 5744 (1999).

133. M. Dijkstra, R. van Roij, and R. Evans, *Phys. Rev. Lett.* **81**, 2268 (1998).

134. M. Dijkstra, R. van Roij, and R. Evans, *Phys. Rev. Lett.* **82**, 117 (1999).

135. W.H. Evers, B. de Nijs, L. Filion, S. Castillo, M. Dijkstra, and D. Vanmaekelbergh, *Nano Lett.* **10**, 4235 (2010).

136. P.J. Camp and M.P. Allen, *J. Chem. Phys.* **106**, 6681 (1997).

137. P.J. Camp, M.P. Allen, and A.J. Masters, *J. Chem. Phys.* **111**, 9871 (1999).

138. R. Blaak, D. Frenkel, and B.M. Mulder. *J. Chem. Phys.* **110**, 11652 (1999).

139. B.S. John, A. Stroock, and F.A. Escobedo, *J. Chem. Phys.* **120**, 9383 (2004).

140. B.S. John and F.A. Escobedo, *J. Phys. Chem. B* **109**, 23008 (2005).

141. B.S. John, C. Juhlin, and F.A. Escobedo, *J. Chem. Phys.* **128**, 044909 (2008).

142. Y. Kallus, V. Elser, and S. Gravel, *Discrete Comput. Geom.* **44**, 245 (2010).

143. S. Gravel and V. Elser, *Phys. Rev. E* **83**, 036703 (2011).

144. A. Haji-Akbari, M. Engel, and S.C. Glotzer, *J. Chem. Phys.* **135**, 194101 (2011).

145. G. Cinacchi and J.S. van Duijneveldt, *J. Phys. Chem. Lett.* **1**, 787 (2010).

146. W.L. Miller, B. Bozorgui, and A. Cacciuto, *J. Chem. Phys.* **132**, 134901 (2010).

147. W.L. Miller and A. Cacciuto, *J. Chem. Phys.* **133**, 234903 (2010).

148. A. Haji-Akbari, M. Engel, and S.C. Glotzer, *Phys. Rev. Lett.* **107**, 215702 (2011).

149. Y. Jiao and S. Torquato, *J. Chem. Phys.* **135**, 151101 (2011).

150. P.F. Damasceno, M. Engel, and S.C. Glotzer, *ACS Nano* **6**, 609 (2012).

151. M. Marechal, U. Zimmermann, and H. Löwen, *J. Chem. Phys.* **136**, 144506 (2012).

152. E.P. Bernard and W. Krauth, *Phys. Rev. Lett.* **107**, 155704 (2011).

153. C.H. Mak, *Phys. Rev. E* **73**, 065104 (2006).

154. A. Jaster, *Phys. Lett. A* **330**, 120 (2004).

155. J.A. Zollweg and G.V. Chester, *Phys. Rev. B* **46**, 11186 (1992).

156. J. Lee and K.J. Strandburg, *Phys. Rev. B* **46**, 11190 (1992).

157. A. Jaster, *Phys. Rev. E* **59**, 2594 (1999).

158. B.J. Alder and T.E. Wainwright, *Phys. Rev.* **127**, 1359 (1962).

159. D. Frenkel and R. Eppenga, *Phys. Rev. A* **31**, 3 (1985).

160. J.A. Cuesta and D. Frenkel, *Phys. Rev. A* **42**, 2126 (1990).

161. K.W. Wojciechowski, A.C. Branka, and D. Frenkel, *Physica A* **196**, 519 (1993).

162. M.A. Bates and D. Frenkel, *J. Chem. Phys.* **112**, 10034 (2000).

163. T. Schilling, S. Pronk, B. Mulder, and D. Frenkel, *Phys. Rev. E* **71**, 036138 (2005).

164. A. Donev, J. Burton, F.H. Stillinger, and S. Torquato, *Phys. Rev. B* **73**, 054109 (2006).

165. Y. Jiao, F.H. Stillinger, and S. Torquato, *Phys. Rev. Lett.* **100**, 245504 (2008).

166. C. Avendaño and F.A. Escobedo, *Soft Matter* **8**, 4675 (2012).

167. C. Vega, E.P.A. Paras, and P.A. Monson, *J. Chem. Phys.* **96**, 9060 (1992).

168. C. Vega, E.P.A. Paras, and P.A. Monson, *J. Chem. Phys.* **97**, 8543 (1992).

169. K.W. Wojciechowski, D. Frenkel, and A.C. Branka, *Phys. Rev. Lett.* **66**, 3168 (1991).

170. M. Dennison, K. Milinković, and M. Dijkstra, *J. Chem. Phys.* **137**, 044507 (2012).

171. K. Milinković, M. Dennison, and M. Dijkstra, *Phys. Rev. E* **87**, 032128 (2013).

172. D. Frenkel, H.N.W. Lekkerkerker, and A. Stroobants, *Nature* **332**, 822 (1988).

173. D. Frenkel and B.M. Mulder, *Mol. Phys.* **55**, 1171 (1985).

174. D. Frenkel, B.M. Mulder, and J.P. McTague, *Phys. Rev. Lett.* **52**, 287 (1984).

175. P.J. Camp, C.P. Mason, M.P. Allen, A.A. Khare, and D.A. Kofke, *J. Chem. Phys.* **105**, 2837 (1996).

176. P. Pfleiderer and T. Schilling, *Phys. Rev. E* **75**, 020402 (2007).

177. A. Donev, F.H. Stillinger, P.M. Chaikin, and S. Torquato, *Phys. Rev. Lett.* **92**, 255506 (2004).

178. M. Radu, P. Pfleiderer, and T. Schilling, *J. Chem. Phys.* **131**, 164513 (2009).

179. G. Odriozola, *J. Chem. Phys.* **136**, 134505 (2012).

180. J.A.C. Veerman and D. Frenkel, *Phys. Rev. A* **45**, 5632 (1992).

181. R. Eppenga and D. Frenkel, *Mol. Phys.* **52**, 1303 (1984).

182. M.A. Bates and D. Frenkel, *Phys. Rev. E* **57**, 4824 (1998).

183. P.D. Duncan, M. Dennison, A.J. Masters, and M.R. Wilson, *Phys. Rev. E* **79**, 031702 (2009).

184. P.D. Duncan, A.J. Masters, and M.R. Wilson, *Phys. Rev. E* **84**, 011702 (2011).

185. L. Onsager, *Ann. New York Acad. Sci.* **51**, 627 (1949).

186. D. Frenkel, *Physics world* **6**, 24 (1993).